

# Slip distribution of the February 6, 2023 Mw 7.8 and Mw 7.6, Kahramanmaraş, Turkey earthquake sequence in the East Anatolian Fault Zone

Sylvain Barbot  $^{\circ}$  \*  $^{\circ}$ , Heng Luo  $^{\circ}$  2, Teng Wang  $^{\circ}$  2, Yariv Hamiel  $^{\circ}$  3, Oksana Piatibratova  $^{\circ}$  3, Muhammad Tahir Javed  $^{\circ}$  4, Carla Braitenberg  $^{\circ}$  4, Gokhan Gurbuz  $^{\circ}$  5

<sup>1</sup>Department of Earth Sciences, University of Southern California, Los Angeles, USA, <sup>2</sup>Peking University, Beijing, China, <sup>3</sup>Geological Survey of Israel, Jerusalem 9692100, Israel, <sup>4</sup>Department of Mathematics and Geosciences, University of Trieste, Italy, <sup>5</sup>Department of Aerospace Engineering, Faculty of Engineering, Zonguldak Bulent Ecevit University, 67100, Zonguldak, Turkey

Author contributions: Sentinel-1 and ALOS-2 processing: H. Luo and T. Wang. Raw GNSS data: G. Gurbuz. GNSS processing: Y. Hamiel and O. Piatibratova. Additional Sentinel-1 processing and modeling: M. T. Javed and C. Braitenberg. Numerical modeling and visualization: S. Barbot. Original draft: All authors.

**Abstract** On February 6, 2023, two large earthquakes occurred near the Turkish town of Kahramanmaraş. The moment magnitude (Mw) 7.8 mainshock ruptured a 310 km-long segment of the left-lateral East Anatolian Fault, propagating through multiple releasing step-overs. The Mw 7.6 aftershock involved nearby left-lateral strike-slip faults of the East Anatolian Fault Zone, causing a 150 km-long rupture. We use remote-sensing observations to constrain the spatial distribution of coseismic slip for these two events and the February 20 Mw 6.4 aftershock near Antakya. Pixel tracking of optical and synthetic aperture radar data of the Sentinel-2 and Sentinel-1 satellites, respectively, provide near-field surface displacements. High-rate Global Navigation Satellite System data constrain each event separately. Coseismic slip extends from the surface to about 15 km depth with a shallow slip deficit. Most aftershocks cluster at major fault bends, surround the regions of high coseismic slip, or extend outward of the ruptured faults. For the mainshock, rupture propagation stopped southward at the diffuse termination of the East Anatolian fault and tapered off northward into the Pütürge segment, some 20 km south of the 2020 Mw 6.8 Elazığ earthquake, highlighting a potential seismic gap. These events underscore the high seismic potential of immature fault systems.

**Non-technical summary** On February 6, 2023, Turkey and Syria were shaken by powerful earth-quakes that caused tremendous damage and loss of life. Earthquakes in this region occur naturally due to the long-term motion of tectonic plates around the Mediterranean Basin. To better understand the circumstance of these tragic events, we analyze remote sensing data that measure the ground displacement caused by these earthquakes. We find that the mainshock was caused by up to 8 m of slip on the East Anatolian Fault, connecting segments that historically ruptured individually. The Mw 7.6 aftershock produced more slip at depth, up to 12 m, on a separate fault. Alarmingly, the Pütürge segment of the East Anatolian Fault remains unbroken, bearing the potential for another Mw 6.8 earthquake.

Özet (Turkish) 6 Şubat 2023'te Türkiye'nin Kahramanmaraş ilçesi yakınlarında iki büyük deprem meydana geldi. Moment büyüklüğü (Mw) 7,8 olan ana şok, sol yanal atımlı Doğu Anadolu Fayı'nın 310 km uzunluğundaki bir bölümünü yırttı ve birçok adımda enerji boşalmasıyla ilerledi. Mw 7.6 artçı şoku, Doğu Anadolu Fay Zonu'nun yakınındaki sol yanal doğrultu atımlı fayları etkileyerek 150 km uzunluğunda bir yırtılmaya neden oldu. Bu iki olay ve Antakya yakınlarındaki 20 Şubat Mw 6.4 artçı sarsıntısı için eş-sismik kaymanın uzamsal dağılımını sınırlamak için uzaktan algılama gözlemlerini kullanıyoruz. Sırasıyla, Sentinel-2 ve Sentinel-1 uydularının optik ve sentetik açıklıklı radar verilerinin piksel takibi, yakın alan yüzey yer değiştirmelerini sağlar. Yüksek oranlı Küresel Navigasyon Uydu Sistemi (GNSS) verileri, her olayı ayrı ayrı sınırlar. Eş sismik kayma, sığ bir kayma açığı ile yüzeyden yaklaşık 15 km derinliğe kadar uzanır. Artçı şokların çoğu, büyük fay kıvrımlarında kümelenir, yüksek eş-sismik kayma bölgelerini çevreler veya yırtılmış fayların dışına doğru uzanır. Ana şok için, yırtılma yayılımı Doğu Anadolu fayının dağınık son noktasında güneye doğru durmuş ve kuzeye, 2020 Mw 6.8 Elazığ depreminin yaklaşık 20 km güneyindeki Pütürge segmentine doğru incelerek potansiyel bir sismik boşluğa dikkat çekmiştir. Bu olaylar olgunlaşmamış fay sistemlerinin yüksek sismik potansiyelinin altını çizmektedir.

Production Editor:
Stephen Hicks
Handling Editor:
Edwin Nissen
Copy & Layout Editor:
Théa Ragon

Reviewed by: Romain Jolivet

Translated by: Musavver Didem Cambaz Rami Alshembari

Received:
March 20, 2023
Accepted:
April 16, 2023
Published:
April 20, 2023

<sup>\*</sup>Corresponding author: sbarbot@usc.edu

في السادس من فبراير 2023, وقع زلزالان كبيران بالقرب من مدينة كهرمان مرعش التركية. تسبب الزلزال ليمتد لحوالي الرئيسي الذي بقوة 7.8 درجة على مقياس العزم الزلزالي في حدوث تمزق على عدة مراحل من حيث الانتشار ليمتد لحوالي 310 كيلومترات على صدع شرق الأناضول ذي الازاحة الجانبية- في الاتجاة الأيسر. بينما تسببت الهزة الارتدادية ذات قوة 7.6 درجة على مقياس العزم الزلزالي في حدوث صدع الزلاقي افقي strike-slip faults بطول 150 كيلومترات على الجانب الأيسر القريب من منطقة صدع شرق الاناضول. في هذه الدراسة, استخدمنا قياسات الاستشعار عن بعد لدراسة التوزيع المكاني المتزلاق المصاحب للزلزال لهذين الحدثين و الهزة الارتدادية في 20 فبراير ذات قوة 6.4 درجة على مقياس العزم الزلزالي بالقرب من انطاكيا. تم تحديد الازاحات السطحية القريبة من المصدر الزلزالي باستخدام بيانات تتبع البكسل او عنصر الصورة لرادار ذات الفتحة الضوئية والاصطناعية للاقمار الصناعية سينتينيل-2 و سينتينيل -1، على التوالي. في حين ان بيانات نظام القمر الصناعي العالمي GNSS عالية التردد استخدمت لتقيد النتائج لكل زلزال على حدة. يمتد الانزلاق المصاحب للزلزال من المصاحب المنطقة المربعي عجز في المستويات الضحلة القريبة من السطح. معظم الهزات الارتدادية تتجمع عند انحناءات الصدع عمق 15 كيلومترات مع عجز في المساوريات الضحلة الصدع المنطقة المنزلاق المصاحب للزلزال أو تمتد خارج منطقة الصدوع. بالنسبة إلى الهزة الرئيسية، ينتهى انتشار جنوب زلزال Pütürge عند نهاية الانتشار لصدع شرق الأناضول وينحصر شمالا في قطع Pütürge على بعد حوالي 20 كيلومترات جنوب زلزال الحداث تشير الى القدرة الزلز الية العالمة لأطمة الصدوع الغير الناضجة.

#### Introduction

The Mediterranean Basin sits in the western section of the Alpine-Himalayan seismic belt, which was formed by the closure of the Tethys Sea (Jackson and McKenzie, 1984; Taymaz et al., 1991; Bozkurt, 2001). The eastern Mediterranean region is the most seismically active region in Europe due to the rapid movement of small tectonic blocks (Malinverno and Ryan, 1986; Faccenna and Becker, 2010; Le Pichon and Kreemer, 2010; Nocquet, 2012). The indentation of the Arabian plate, the tectonic escape of Anatolia, and the opening of the Aegean Sea accompanied by slab rollback at the Hellenic Trench orchestrate a large-scale rotation accommodated by major transform faults (Jolivet et al., 2013; Faccenna et al., 2014; Barbot and Weiss, 2021). The indentation of the Arabian plate forms a triple junction with slip partitioning among the North Anatolian Fault (NAF), the East Anatolian Fault (EAF), and the Main Recent Fault (Talebian and Jackson, 2002; Vernant et al., 2004; Reilinger et al., 2006). The NAF is a 1,200 km-long, mature, right-lateral strike-slip fault extending from the Karliova triple junction to the Sea of Marmara (Ambraseys, 1970; Armijo et al., 1999; Hubert-Ferrari et al., 2002; Le Pichon et al., 2016; Güvercin et al., 2022). The EAF, a conjugate, 300 km-long left-lateral fault, extends southwards and branches out diffusely to the Dead Sea Fault (DSF) and the Cyprus Arc to the southwest (Duman and Emre, 2013). The EAF connects multiple segments with a low long-term slip rate (Aktug et al., 2016; Cavalié and Jónsson, 2014) separated by major releasing bends and step-overs (Duman and Emre, 2013; Güvercin et al., 2022), making it relatively immature compared to the NAF and other continental strike-slip faults (Wesnousky, 1988). Farther south, the left-lateral DSF is the boundary fault accommodating the northward migration of the Arabian plate (Garfunkel et al., 1981; Hamiel and Piatibratova, 2021).

The motion of these tectonic plates is modulated by the frictional resistance of faults in the brittle crust, leading to seismic cycles. The NAF ruptured in a long sequence of earthquakes in the 20<sup>th</sup> century, starting with the 1939 Erzincan earthquake, and ending with the 1999 Mw 7.9 Izmit and Mw 7.2 Düzce earthquakes near Istanbul in Western Turkey (Ambraseys, 1970; Hartleb

et al., 2003; Bohnhoff et al., 2016). The EAF featured several notable earthquakes during the last century, with the 1905 Mw 6.8, the 1971 Mw 6.7, the 2010 Mw 6.1, and the 2020 Mw 6.8 earthquakes, but the section south of Elaziğ has remained locked for more than a century (Hubert-Ferrari et al., 2020; Duman and Emre, 2013). Previous large earthquakes in this section include the 1114 M 6.9, 1795 Mw 7.0, 1872 Mw 7.2, and 1893 Mw 7.1 ruptures (Ambraseys, 2009; Güvercin et al., 2022), all bounded by major (releasing) fault bends (Duman and Emre, 2013). Since then, the fault has remained mostly locked, slowly accumulating stress, until it finally unzipped in a continuous rupture in 2023, generating a powerful Mw 7.8 earthquake (Dal Zilio and Ampuero, 2023; Melgar et al., 2023).

The February 6, 2023 Kahramanmaraş earthquake, the largest seismic event in Turkey since 1939, ruptured the south-western segments of the EAF (Figure 1). The powerful mainshock initiated a long aftershock sequence including the Mw 7.6 Elbistan earthquake just 9 hours later on the east-west trending left-lateral Cardak fault in the East Anatolian Fault Zone (EAFZ) and the February 20, Uzunba Mw 6.4 aftershock near Antakya (hereafter, called the Antakya aftershock), where the EAF bifurcates offshore towards the Cyprus arc. Such a sequence of large earthquakes on nearby faults within hours of each other has no equivalent in a continental setting, especially considering the similar source mechanisms. The mainshock and its large aftershocks destroyed or severely damaged some 160,000 buildings, killed more than 50,000 people, displaced 200,000 more, and affected 14 million people across Turkey and Syria.

In this study, we combine spaceborne geodesy and seismological data to constrain the slip distribution of the 2023 Kahramanmaraş earthquake sequence to address first-order questions regarding the mechanisms of rupture propagation and arrest in the EAFZ. We constrain the near-field deformation of the February 6 Mw 7.8 and Mw 7.6 earthquakes using cross-correlation of Sentinel-2 optical data (ForM@Ter, 2023) and synthetic aperture radar (SAR) images, and Advanced Land Observing Satellite (ALOS) data before and after the February 6 earthquakes. We use high-rate Global Navigation Satellite Systems (GNSS) data to constrain the surface displacement caused by these earthquakes within

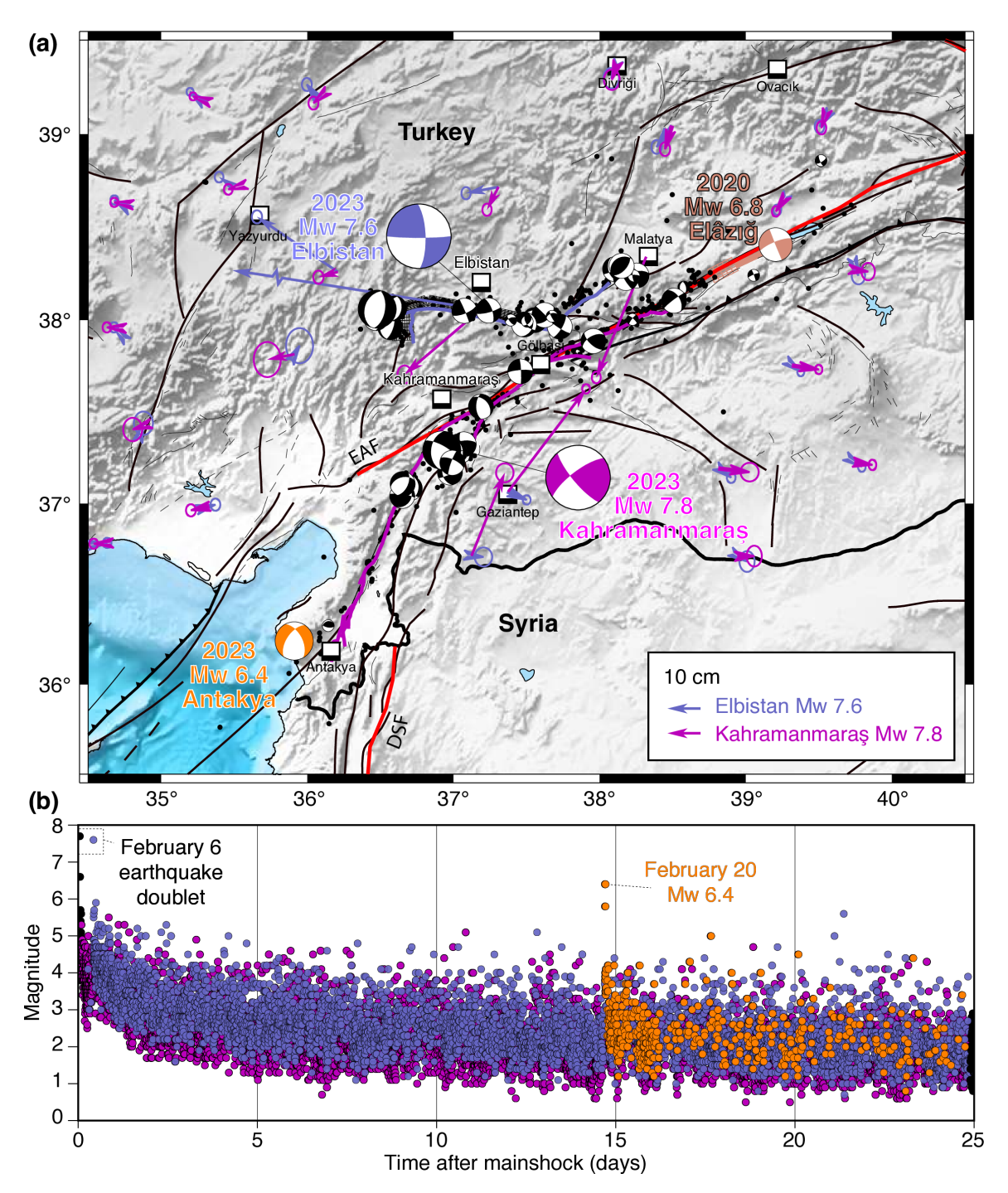


**Figure 1** Tectonic setting and crustal deformation of the East Anatolian Fault (EAF) on February 6, 2023. a) The aftershocks (black dots, Lomax, 2023) and the focal mechanisms of earthquakes of moment magnitude greater than 4 (beach balls) illuminate the ruptures of the Kahramanmaraş Mw 7.8 (purple) and the Elbistan Mw 7.6 (blue) earthquakes. The fault offsets (Reitman et al., 2023) indicate the extent of the ruptures. The EAF and Dead Sea Fault (DSF), plate-boundary faults are shown in red. Major and minor faults are shown in thick and thin black lines, respectively (Emre et al., 2018). The focal mechanisms are from the Disaster and Emergency Management Presidency (AFAD) catalog for the day of February 6, 2023 (https://deprem.afad.gov.tr/event-catalog). The topography is from the Global Multi-Resolution Topography Synthesis (GMRT) v3.7 (Ryan et al., 2009). b) Time series of aftershocks magnitude in the days following the mainshock (purple for aftershocks within 20 km of the EAF, blueish for aftershocks within 20 km of the Mw 7.6 rupture, and orange for earthquakes within 20 km of the Mw 6.4 Antakya aftershock). The Mw 7.8 mainshock and the Mw 7.6 aftershock just 9 hours later form an earthquake double. The February 20, 2023 Mw 6.3 aftershock occurs at the southern termination of the EAF.

a 200 km radius. We ensure that the fault geometry at depth follows the distribution of relocated aftershocks (Lomax, 2023). The mainshock rupture is bounded to the south by the February 20, Mw 6.4 Antakya earthquake and the transition between the EAF

and Antakya Fault that propagates into the Mediterranean Basin (Figure 2). We constrain the rupture of the Mw 6.4 aftershock using synthetic aperture radar interferometry (InSAR). The mainshock rupture stopped south of the Pütürge segment some 30 km south of the

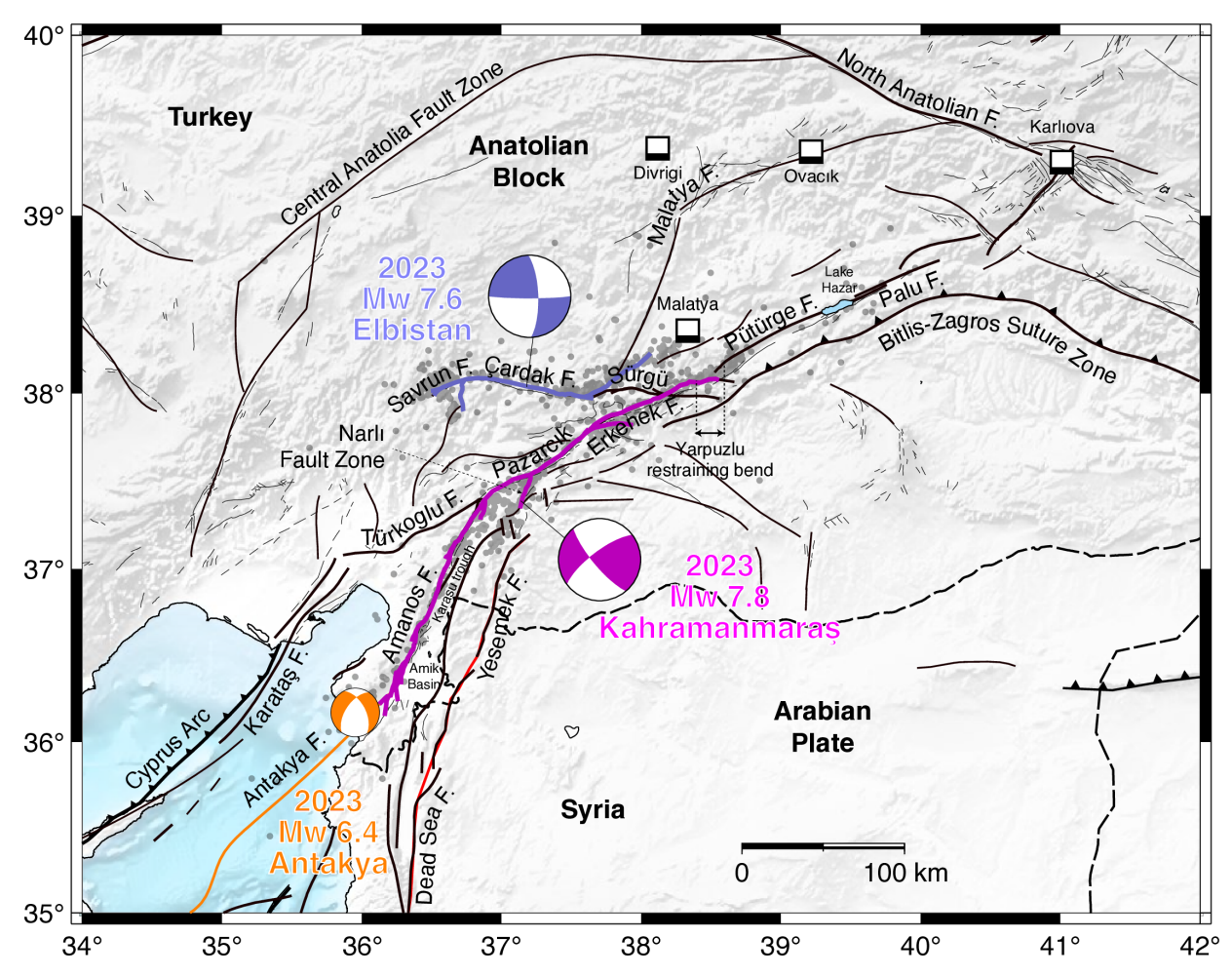


**Figure 2** Simplified tectonic map of the East Anatolian Fault Zone after Duman and Emre (2013) and Emre et al. (2018). The East Anatolian Fault consists of a succession of discontinuous segments. The Mw 7.8 mainshock ruptured the Amanos, Pazarcık, and Erkenek segments and stopped at the Yarpuzlu restraining bend. The Mw 7.6 aftershock ruptured the Savrun Fault, the Çardak Fault, and propagated toward Malataya along a structure between the Sürgü Fault and the Malatya Fault. Fault is abbreviated to "F." to save space. The February 20, 2023 Mw 6.4 aftershock took place near the Antakya Fault towards the Mediterranean Basin. The background seismicity represents the aftershocks within 2 days of the mainshock (Lomax, 2023).

2020 Mw 6.8 Elâziğ earthquake (Pousse-Beltran et al., 2020a; Ragon et al., 2021; Konca et al., 2021), leaving a potential seismic gap in the intervening region.

The coseismic slip of these earthquakes illuminates some important characteristics of the brittle crust in the EAFZ. Along the EAF, the slip distribution is characterized by a shallow slip deficit, a maximum coseismic slip of 8 m between 3 and 7 km depth, and a bottom depth of 18 km depth — presumably including much afterslip. Along the strike direction, coseismic slip is maximum at the center of planar segments and tapers at the segment boundaries. The small-magnitude aftershocks cluster at the segment boundaries and at the periphery of regions of high coseismic slip. Along the Çardak fault, the coseismic slip of the Mw 7.6 aftershock is relatively uniform with 11 m from the surface to 7 km depth, vanishing at 12 km depth.

# **Data processing methods**

We constrain the slip distribution of the Kahramanmaraş and the Elbistan earthquakes using spacegeodetic data from the Sentinel-1 and Sentinel-2 satellites and from GNSS measurements. Sentinel-1 SAR provides amplitude and phase images of the crustal deformation surrounding the earthquakes. Although the phase measurements are more sensitive, they are sometimes unavailable near the fault trace due to decorrelation. In this case, the cross-correlation of amplitude data provides key constraints for the near-field surface displacements and fault slip. Cross-correlation of optical Sentinel-2 data provides similar constraints. Unlike the space geodetic data, the temporal resolution of the GNSS data allows us to constrain the displacements caused by individual earthquakes. For the Antakya Mw 6.4 aftershock, we make use of the greater sensitivity of the Sentinel-1 SAR phase and constrain the slip distribution with the inversion of the Sentinel-1 interferograms. Below, we describe the data processing to constrain crustal deformation.

#### **GNSS data processing**

We use GNSS observations from 51 Continuously Operating Reference Stations in Turkey (CORS-TR) with 1 Hz

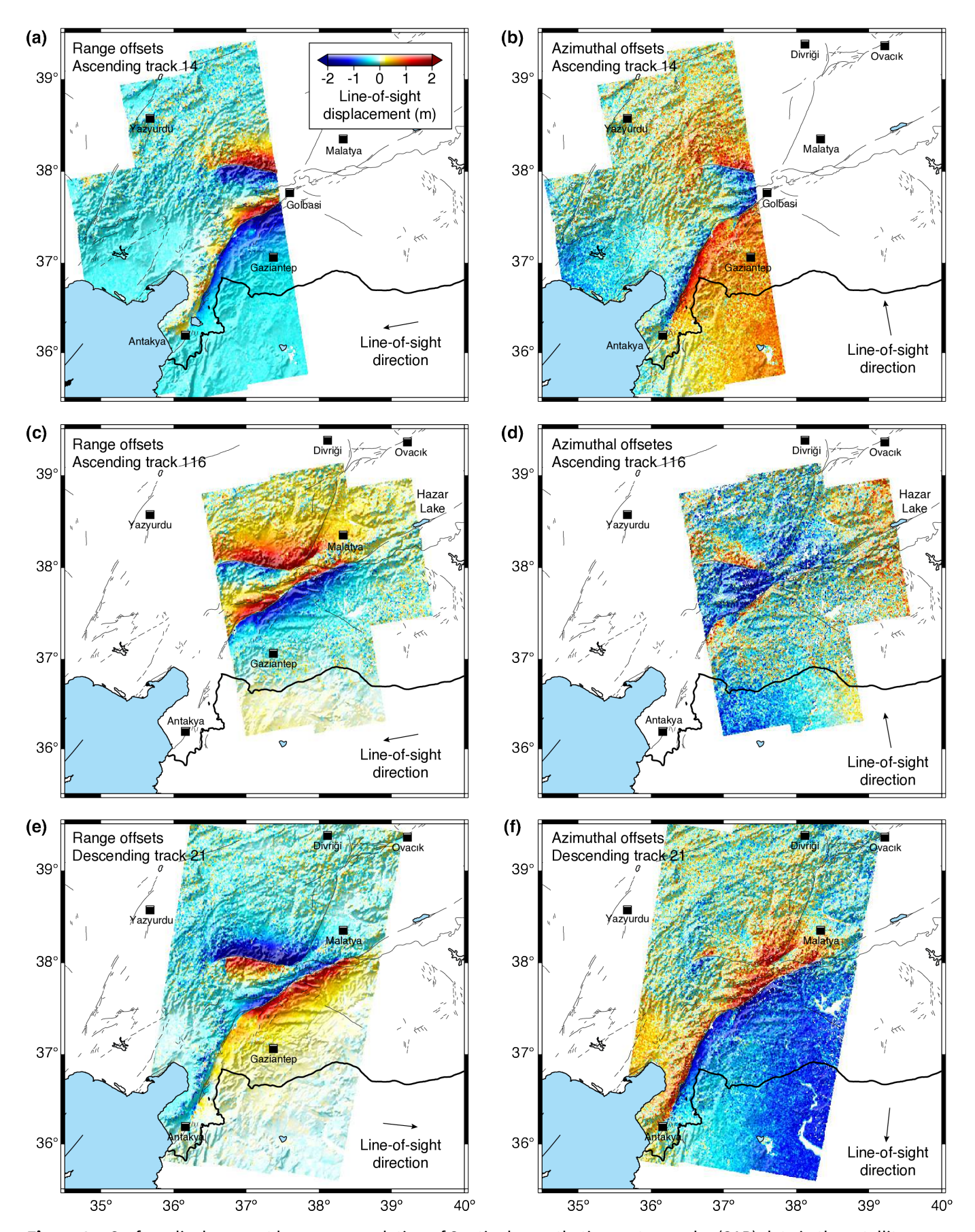


**Figure 3** Surface displacement by cross-correlation of Sentinel-1 synthetic aperture radar (SAR) data in the satellite range and azimuth directions. A) Range (line-of-sight) offsets of Sentinel-1 ascending track 14 acquired on January 28, 2023, and February 9, 2023. B) Azimuthal (track-parallel) offsets for track 14. C) Range offsets for ascending track 116. D) Azimuthal offsets for track 116. E) Range offsets for descending track 21. F) Azimuthal offsets for track 21. The displacement component measured by the offsets is indicated by the black arrow.

frequency and additional 17 continuous stations around Turkey, twelve of which belonging to the International GNSS Service (IGS) network. For the GNSS raw data processing, we use the GAMIT/GLOBK package, version 10.71 (Herring et al., 2018). GAMIT uses a priori data of satellite and station locations and obtains the position and baseline solutions for each session (a day or less). GLOBK uses a Kalman filter, combines all data, and creates a time-series solution for the positions of all stations.

We processed all GNSS data between February 3 and February 9 and obtained daily positions for the first three days before the first Mw 7.8 earthquake on February 6, 01:17 (UTC time) and for the last three days after the second Mw 7.6 earthquake on 10:24 (UTC time) (Figure S1). The February 6<sup>th</sup> data was divided into several sessions. The first session was until 01:16 (UTC time). The time between the two earthquakes was divided into four hours sessions and the same was done after the second earthquake. We calculate the coseismic displacements using the differences in station positions obtained by the before- and after-earthquake sessions. For the first earthquake, we averaged the preearthquake session solution with the February 5th daily solution. The resulting coseismic displacements are shown in Figure 1. The coseismic offsets for the Kahramanmaraş mainshock and the Mw 7.6 Elbistan aftershock are listed in Tables S1 and S2, respectively.

The displacement field is compatible with a left-lateral motion for both events. Station EKZ1 near Elbistan is located 2 km from the Çardak fault that hosted the Mw 7.6 aftershock, revealing up to 4.4 m of westward displacement.

#### Sentinel-1 data processing

We collect Sentinel-1 SAR images spanning the 2023 Mw 7.8 and Mw 7.6 earthquakes in the ascending tracks 14 (AT14) acquired on January 28, 2023, and February 9, 2023, and 116 (AT116) acquired on February 4, 2023, and February 28, 2023, and the descending track 21 (DT21) acquired on January 29, 2023 and February 10, 2023. Because of the large-magnitude deformation caused by the two main events, the near-field fringes in the InSAR interferograms are too dense to unwrap reliably. Therefore, we rely on pixel-offset tracking to measure the coseismic surface deformation caused by these two events (Wang et al., 2014, 2018). The crosscorrelation of the Sentinel-1 SAR amplitude images is shown in Figure 3. For the purpose of inversion, we ignore the regions with a correlation coefficient lower than 0.3. Track DT21 captures the surface trace of the two ruptures continuously. Track AT14 provides additional coverage of the western half of the affected region. The slightly different look directions of tracks DT21 and AT14 allow us to constrain two components of surface deformation. Track AT116 is particularly useful because it constrains crustal deformation along the EAF on the Pütürge segment from Malatya to Lake Hazar that separates the 2023 Mw 7.8 mainshock from the 2020 Mw 6.8 Elazığ ruptures, allowing us to probe the mechanism of northeast rupture arrest.

For the February 20, 2023 Mw 6.4 aftershock near Antakya, we use the interferogram based on SAR images acquired on February 9, 2023, and February 21, 2023, along the ascending track 14 (AT14) and the interferogram based on SAR images acquired on February 10, 2023, and February 22, 2023, on descending track 21 (DT21). With these acquisition dates, the observed deformation includes also the local Mw 5.5 aftershock. We produce the interferograms through the LicSBAS platform (Morishita et al., 2020; Lazecky et al., 2020) and correct for atmospheric perturbations using the GPS-based iterative tropospheric decomposition model GACOS (Yu et al., 2018b,a). We apply the topographic phase correction included in LicSBAS, which uses the digital elevation model from the Shuttle Topography Radar Mission (Farr et al., 2007). The unwrapping is done with the Statistical-cost, Network-flow Algorithm for Phase Unwrapping (Chen and Zebker, 2002). The unwrapped interferograms are shown in Figure 4, revealing crustal deformation to the southwest of the Mw 7.8 mainshock rupture, indicating the propagation of seismic unrest toward the Cyprus Arc, compatible with the distribution of aftershocks (Figures 1 and 2).

#### **ALOS-2 data processing**

We process the ALOS-2 SAR images provided by Japan Aerospace Exploration Agency (JAXA) using the In-SAR Scientific Computing Environment (ISCE) software (Rosen et al., 2012). Thanks to the large ground coverage with a swath width of ~350 km of ScanSAR mode, the whole deformed area of the Mw 7.8 and Mw 7.6 events is imaged by single interferograms in ascending track on September 5, 2022, and February 20, 2023, and descending track on September 16, 2022, and February 17, 2023 (Figure 5). The post-seismic ALOS-2 ascending image was acquired at 21:28 on February 20, 2023 (UTC), after the Mw 6.4 aftershock that occurred at 17:04 on the same day. However, this ascending ALOS-2 interferogram does not cover area most affected by the Mw 6.4 event, which is farther to the south. The topographic component in the interferogram is calculated and removed using the Shuttle Topography Radar Mission digital elevation model. The ionospheric effects are corrected using the split-spectrum method (Barbot et al., 2008b; Liang et al., 2019). The large wavelength of the ALOS-2 data (~24 cm versus 5.5 cm for Sentinel-1) reduces the phase gradient, allowing phase unwrapping near the fault trace. We unwrap the phase using the Statistical-cost, Network-flow Algorithm for Phase Unwrapping (Chen and Zebker, 2002), masking the regions with coherence less than 0.3 or phase aliasing, and manually correcting the unwrapping errors.

#### Sentinel-2 data

We use cross-correlation of Copernicus Sentinel-2 satellite imagery at 10 m spatial resolution before and after February 6, 2023, to estimate the surface horizontal displacements caused by the Mw 7.8 and Mw 7.6 earthquakes (ForM@Ter, 2023). These data are provided by Data Terra and its solid-Earth data hub

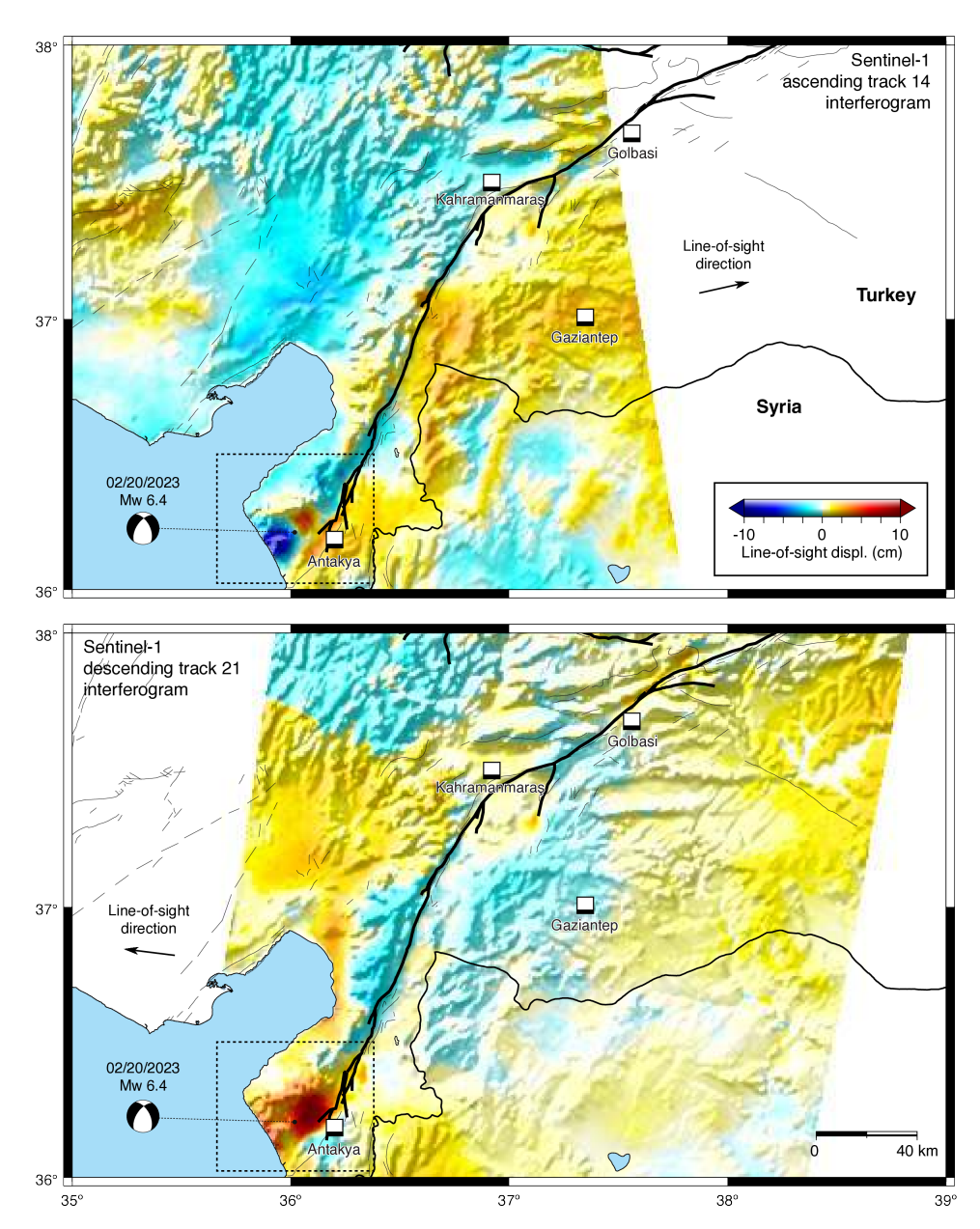


**Figure 4** Sentinel-1 unwrapped interferograms of the February 20, 2023 Mw 6.4 aftershock near Antakya, Turkey. a) Interferogram of ascending track 14, based on SAR images acquired on February 9, 2023 and February 21 2023. b) Interferogram of descending track 21 based on SAR images acquired on February 10, 2023 and February 22, 2023. The dashed rectangle indicates the region most affected by crustal deformation.

ForM@Ter (Provost et al., 2022). The pixel tracking dataset was created with the open-source photogrammetry library MicMac (Rosu et al., 2015; Rupnik et al., 2018). The displacement field is a composite of 10 images acquired on January 25, 2023, and February 9, 2023, consisting of the tiles T36SYF, T36SYG, T37SBA, T37SBB, T37SBC, T37SBV, T37SCB, T37SCC, T37SDB T37SDC.

Pixel tracking of Sentinel-2 optical images provides a continuous measurement of the Mw 7.8 mainshock rupture and of most of the Mw 7.6 aftershock surface trace (Figure S2). However, the data seem affected by nontectonic signals, presumably due to changes in cloud cover and snow between the two acquisitions. Therefore, we limit the use of these data to constrain the fault trace and the amount of near-surface slip.

## Slip distribution

The Mw 7.8 mainshock initiated on the Narlı Fault Zone that bounds the Narlı basin, north of the Karasu trough (Figures 1 and 2). The rupture continued along the East Anatolian Fault, propagating bilaterally into the Amanos segment to the south and into the Pazarcık and Erkenek segments to the north (Melgar et al., 2023). The surface rupture stopped just northeast of the Yarpuzlu restraining bend. There is no visible surface break along the Pütürge segment even though aftershocks extend to the southern limit of the 2020 Mw 6.8 Elazığ rupture.

The Mw 7.6 aftershock nucleated in the middle of the Çardak Fault and propagated westward to the Savrun Fault and eastward across the so-called Nurhak complexity (Duman and Emre, 2013) along an immature

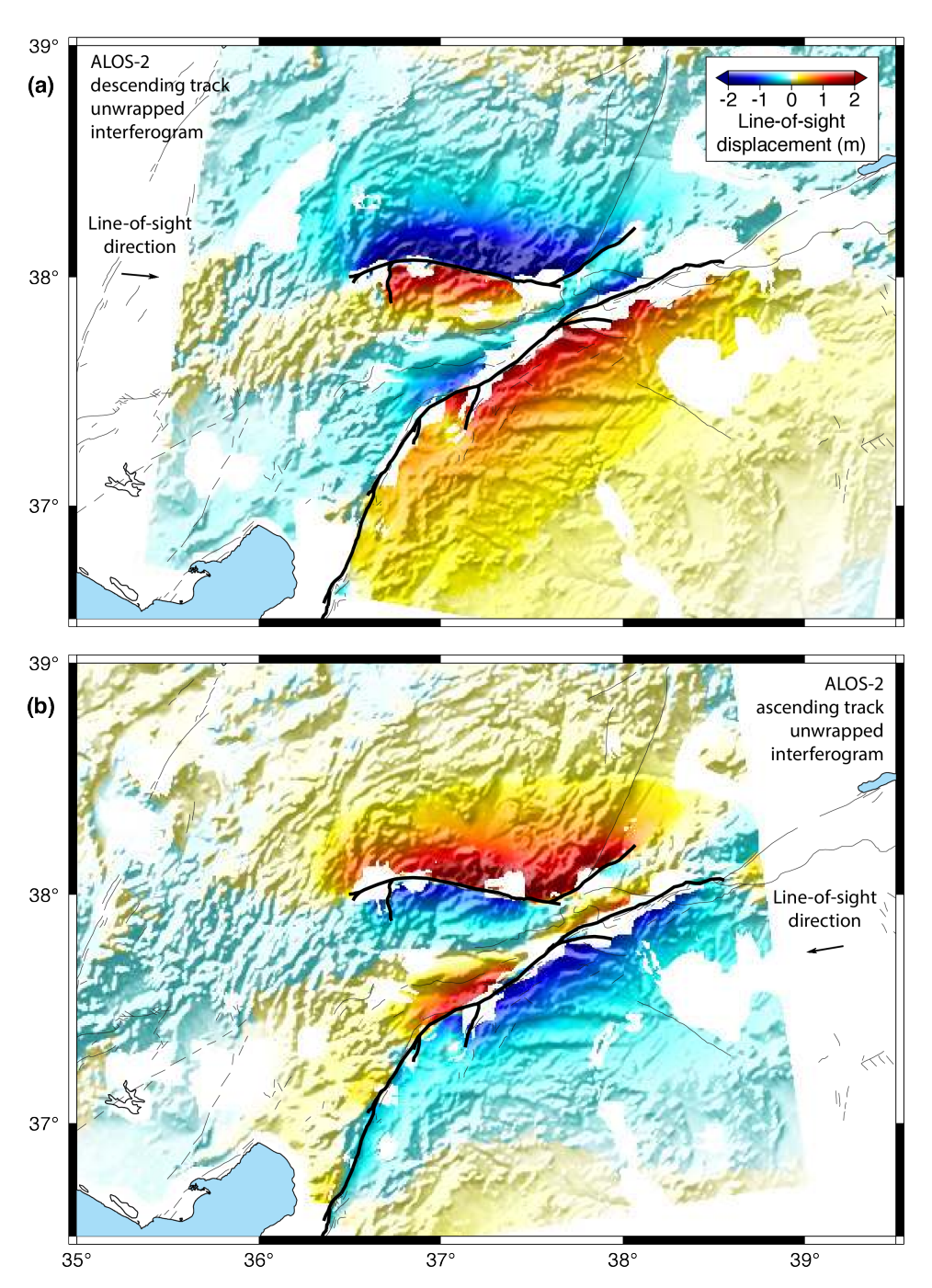


**Figure 5** Coseismic unwrapped interferograms converted to line-of-sight displacements from the a) descending and b) ascending tracks of the ALOS-2 satellite. The color scale indicates the amount of displacement along the line-of-sight direction (arrow). Some near-field phase information is removed to avoid bias from aliasing. The regions causing unwrapping errors are manually removed, appearing as white patches. The descending interferogram is the phase difference from SAR images acquired on September 16, 2022, and February 17, 2023. The ascending interferogram is based on acquisitions on September 5, 2022, and February 20, 2023.

fault between the Malatya and the Sürgu faults (Melgar et al., 2023). The Mw 7.6 aftershock triggered a sequence of additional aftershocks including normal faulting earthquakes near the Savrun Fault (Figure 1). The aftershocks cluster north of the Çardak Fault, indicating a north dipping fault.

We constrain the trace of the rupture surface of the February 6 earthquakes by examination of the displacement discontinuity in the near-field optical and SAR amplitude pixel-tracking, and InSAR data (Figures 3, S2, and 5). There is no indication of slip on the Sürgu

fault connecting the Çardak fault to the EAF. The Mw 7.8 mainshock and the Mw 7.6 aftershock occurred on disconnected faults. The long streak of seismicity east of the Karasu trough and south of the Narlı Basin is not associated with detectable surface displacements.

We simplify the geometry by considering 8 and 5 segments of uniform orientation for the Mw 7.8 mainshock and the Mw 7.6 aftershock, respectively (Table 1). We extend the fault planes to a depth of 20 km running through the relocated seismicity (Lomax, 2023). For the Mw 7.8 mainshock, we extend the model to include the

Segment name	Longitude	Latitude	Length (km)	Width (km)	Strike (°)	Dip (°)
Kahramanmaraş Mw 7.8 mainshock						
S. Amanos	36.204930	36.265216	104	20	25	90
N. Amanos	36.668276	37.124694	40	20	35	90
Pazarcık	36.895917	37.415278	50	20	64	90
Pazarcık	37.399309	37.620637	34	20	50	90
Erkenek	37.668186	37.820997	50	20	69	90
Pütürge	38.196738	37.987298	58	20	63	90
İzci	38.318033	38.037183	20	20	79	90
Narlı	37.129175	37.337908	14	20	20	90
Elbistan Mw 7.6 aftershock						
Savrun	36.520130	38.005252	28	20	74	110
Çardak	36.824423	38.080845	70	20	102	110
Gök Hill	37.607312	37.961607	24	20	59	90
Söğüt	37.839693	38.075523	46	20	54	90
Yeşilköy	36.728407	37.898624	18	20	0	130
Antakya Mw 6.4 aftershock						
Antakya	36.229999	36.207670	25	25	237	55

**Table 1** List of segments of uniform orientation used for the finite slip distribution of the February 6, 2023 Kahramanmaraş Mw 7.8 mainshock and Elbistan Mw 7.6 aftershock, for the February 20, 2023 Antakya Mw 6.4 aftershock. The width is for the down-dip distance.

Pütürge segment to test whether any blind slip occurred north of the surface rupture. We use vertical faults for the Mw 7.8 mainshock, which is sufficient to follow the distribution of aftershocks. However, small variations of dip of  $\pm 15^{\circ}$  are admissible.

For the Mw 7.6 aftershock, we include a normal fault at the western end of the Çardak Fault to capture a displacement discontinuity perpendicular to the main trace compatible with the concentration of aftershock with a normal faulting focal mechanism (Figure 1). We assume a dip angle of 60° for the Çardak Fault, compatible with the distribution of aftershocks in this location. We use a dip angle of 50° for the normal fault south of the Savrun Fault, also compatible with the distribution of aftershocks.

We discretize the fault planes with  $2 \times 2 \text{ km}^2$  patches and use the Green's function relating the fault strike-slip and dip-slip components to surface displacement for an elastic half-space (Okada, 1992). To reduce the number of data points used in finite-source modeling, we downsample the observations using a quadtree (e.g., Jónsson et al., 2002; Fialko, 2004). We invert for the slip distribution using regularized least-squares by imposing a smooth distribution of slip enforced by a Laplacian operator (Huiskamp, 1991). We use an L-curve (Figure S3) to estimate the optimal smoothing constraints (Aster et al., 2012). The resolution of the inversion deteriorates rapidly with depth, with an average of 45% in the first 2 km dropping to 1-3% at 6-7 km depth, as is typical with geodetic constraints (Barbot et al., 2008a, 2013; Sathiakumar et al., 2017). The inferred slip distribution represents a spatial average that masks short-wavelength variations. However, the bulk features of the model, such as the along-strike variations, can be determined more reliably.

The comparison between the observations and the forward model associated with the finite-source inversion is shown in Figures S4 and S5. There are high-frequency residuals along the fault traces (e.g., Fig-

ures S4c,f) due to the simplifying assumption of a piecewise linear fault trace. In reality, the faults run through numerous bends and jogs at fine scales that are not captured by our geometrically simple model. There are one-sided residuals in the near field of the Çardak fault and the central EAF in the Sentinel-1 DT21 range offset (Figure S4c) that would imply a different fault dip angle. However, the other datasets are explained well in the same location.

Overall, there is a good agreement between the various datasets considered. The model explains the GNSS displacements for the Mw 7.8 mainshock and Mw 7.6 aftershock particularly well, with a variance reduction of 85% and 97%, respectively (Figure S4a-f). The model variance reduction for the Sentinel-1 pixel-tracking data ranges from 37 to 61% due to a large background noise that is common for this type of data (Leprince et al., 2007). The variance reduction for the ALOS-2 interferograms is 73% and 80% for the ascending and descending tracks, respectively. The variance reduction for the Sentinel-2 optical data is only 12%, due to large measurement errors associated with cloud and snow cover (Figure S6). However, these data are useful to constrain the distribution of shallow fault slip.

The resulting slip distributions for the Mw 7.8 main-shock and the Mw 7.6 aftershock are shown in Figure 6. Along the EAF, coseismic slip is maximum between 3 and 7 km depth, tapering off from 8 to 14 km depth. Fault slip is mostly left-lateral with small changes of dip near the surface. Assuming a uniform shear modulus of 30 GPa, we find a geodetic moment of  $5.4 \times 10^{20}$  Nm corresponding to Mw=7.8. The slip distribution is highly segmented and relatively uniform within segments of uniform strike angle, revealing asperities of large slip within the South Amanos, North Amanos, Pazarcık, and Erkenek segments. Slip is the largest along the Pazarcık segment, reaching a maximum of 8 m. Along the South Amanos segment, slip reaches 4 m, tapering off to the southwest. To the northeast, the surface rupture shows

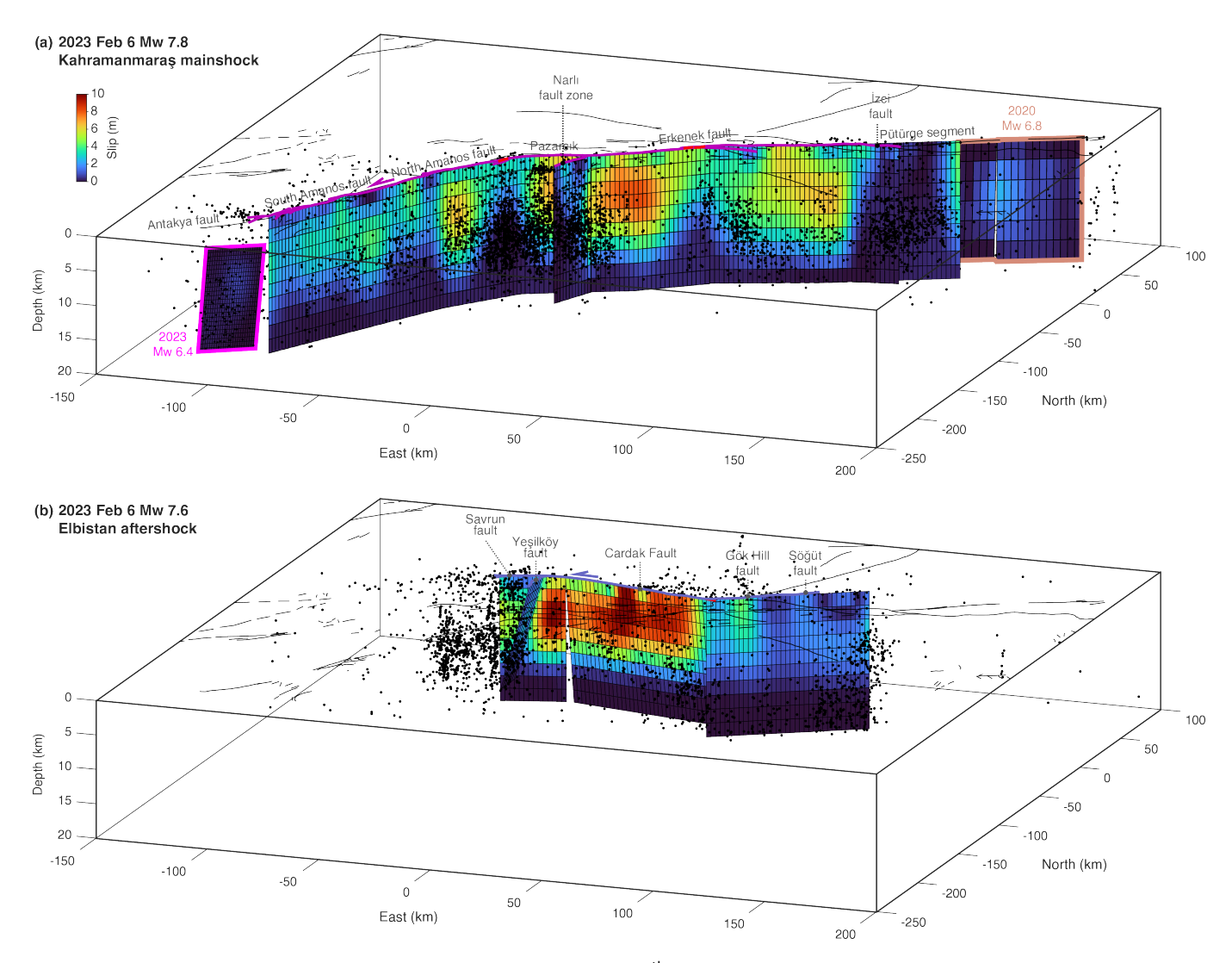


**Figure 6** Coseismic slip distribution of a) the 2023 February 6<sup>th</sup> Mw 7.8 Kahramanmaraş mainshock, the February 20th Mw 6.4 aftershocks (purple), and the 2020 Mw 6.8 Elazığ earthquake (Pousse-Beltran et al., 2020a) (light brown) and b) the 2023 February 6<sup>th</sup> Mw 7.6 Elbistan aftershock. The maximum slip of 8 m on the EAF concentrates between 3 and 7 km depth, highlighting a shallow slip deficit. The maximum slip on the Çardak fault during the Mw 7.6 aftershock is 11 m from the surface to 7 km depth. The small-magnitude aftershocks (Lomax, 2023) concentrate at segment boundaries and around the regions of high coseismic slip.

a bifurcation to the İzci segment. However, this is not accompanied by much fault slip at depth.

The rupture of the Mw 7.6 aftershock is more compact, mostly confined to the Çardak fault with a maximum slip of 12 m from the surface to 7 km depth. The slip tapers off from 8 to 12 km, shallower than along the EAF. Slip along the northeast-striking Gök Hill and Söğüt segments between the Malatya and Sürgü faults is limited to at most 5 m. Slip on the south-striking Yeşilköy normal fault reaches 2 m. Assuming a uniform shear modulus of 30 GPa, we find a geodetic moment of  $3.3 \times 10^{20}$  Nm corresponding to Mw=7.6.

# The February 20, 2023, Mw 6.4 Antakya aftershock

We now examine the southern termination of the mainshock rupture, which is associated with a large cluster of aftershocks. Specifically, we focus on the crustal deformation caused by the February 20, 2023, Mw 6.4 aftershock near Antakya that was captured by Sentinel-1 data. Focusing on the small footprint most affected by the Mw 6.4 aftershock, we determine the position, orientation, dimension, and slip vector based on the In-SAR data in a Bayesian inversion (Bagnardi and Hooper, 2018; Javed et al., 2022). These data can be explained well by a fault striking  $237\pm5^{\circ}N$  with a dip angle of  $55\pm5^{\circ}$ . The fault orientation falls within the large cloud of aftershock hypocenters and aligns well with the Antakya Fault that runs toward the Cyprus Arc.

Using the inferred geometry, we invert for a finite slip distribution applying a non-negative least square inversion (Jónsson et al., 2002), with a discretization of the fault into  $1 \times 1 \,\mathrm{km^2}$  patches. Slip is allowed to have along-strike and down-dip components. We use the L-curve (Aster et al., 2012) to resolve the trade-off between misfit and roughness (Figure S8). The data used for the inversion are defined by the dashed frame in Figure 4. We use the ascending and descending interferograms jointly to constrain the slip distribution. The

rupture extends along the strike with a length of 25 km, and a downdip distance of 25 km. The maximum slip of 0.93 m occurs at a depth of 8.3 km, with a rake of -12°, corresponding to dominantly left-lateral slip, with the area affected by greater slip extending down-dip towards the northeast (Figure 6). The comparison between the Sentinel-1 observations for tracks AT14 and DT21 and the forward model for the Mw 6.4 Antakya aftershock is shown in Figure S7.

#### **Discussion**

The slip distribution of the Kahramanmaras seismic sequence brings light into the processes of earthquake rupture propagation and arrest and the properties of the seismogenic zone in the continental crust. Even though the rupture reaches the surface in many locations, the slip distribution is overall characterized by a shallow slip deficit (Figure 7), similar to many large earthquakes in the continental crust (Fialko et al., 2005; Wei et al., 2015; Qiu et al., 2020). For the EAF, the slip reaches a maximum between 3 and 7 km depth. While the maximum slip reaches 8 m at depth, the surface slip peaks only at 6 m, indicating a 25% slip deficit. The coseismic slip of the 2020 Mw 6.8 Elazığ earthquake is even more confined, leading to a 60% slip deficit (Figure 7f). The peak of 12 m of slip at 4 km depth on the Çardak fault leads to a 25% slip deficit as well (Figure 7e). For the system to conserve mass, slip must accumulate at different parts of the seismic cycle as afterslip (Barbot et al., 2009a; Rousset et al., 2012; Rollins et al., 2015; Tang et al., 2020) or more slowly during the interseismic phase (Barbot et al., 2013; Kaneko et al., 2013; Cetin et al., 2014; Bilham et al., 2016; Rollins et al., 2018), or by straining a wider region surrounding the fault. It is possible that much of the shallow slip occurs aseismically during the intervening days between the mainshock and the remote-sensing data acquisition.

The shallow slip deficit is broadly compatible with the thermal activation of rate-, state-, and temperaturedependent friction in the continental crust (Barbot, 2019a; Wang and Barbot, 2020). Most rocks exhibit steady-state velocity-strengthening behavior at room temperature, transitioning to velocity-weakening at temperatures relevant to the mid-crust, for example, pyroxene (Tian and He, 2019), amphibole (Liu and He, 2020), blueschist (Sawai et al., 2016), granite (Mitchell et al., 2016), serpentinite (Takahashi et al., 2011), biotite (Lu and He, 2014, 2018), shale (An et al., 2020), and samples of mixed composition taken from natural faults (Boulton et al., 2014; Rabinowitz et al., 2018; Valdez II et al., 2019; den Hartog et al., 2021). The shallow velocity-strengthening layer can also be caused by the presence of granular material associated with sediments or a damage zone. Another explanation is the broadening of the deformation zone surrounding the fault, such as a flower structure or distributed plasticity (Fialko et al., 2002; Hamiel and Fialko, 2007; Barbot et al., 2008a, 2009b; Cochran et al., 2009). However, the spatial resolution of the geodetic data considered is limited to 2 km, and we cannot resolve the distribution of deformation below this length scale.

The distribution of seismicity spans a markedly greater depth range than coseismic slip, extending down to at least 20 km depth in this region (Bulut et al., 2012; Pousse-Beltran et al., 2020b). It is therefore useful to discriminate the seismic layer from the seismogenic zone defined as the depth of nucleation and initial propagation of large earthquakes. The seismic layer represents the maximum depth of micro-seismicity (e.g., Shearer et al., 2005; Nazareth and Hauksson, 2004), which is caused by small-scale heterogeneities in composition, fluid pressure, normal stress, texture, and fault orientation. Ultimately, the seismic layer may terminate at the brittle-ductile transition. In contrast, the seismogenic zone is controlled by the stability of frictional sliding (Blanpied et al., 1995), which may be entirely controlled by the distribution of frictional properties (Ruina, 1983; Rice and Ruina, 1983; Rubin and Ampuero, 2005; Barbot, 2019b; Wang and Barbot, 2020, 2023).

The coseismic slip distribution constrains the depth of the seismogenic zone. However, during the rupture of large earthquakes, coseismic slip propagates into the velocity-strengthening domains due to the concentration of static and dynamic stresses near the free surface (e.g., Barbot et al., 2012; Jiang and Lapusta, 2016; Jiang et al., 2022) and is affected by enhanced weakening mechanisms (Di Toro et al., 2011). As a result, the unstable-weakening region that forms the seismogenic zone is presumably much narrower than the depth extent of coseismic slip.

The distribution of aftershock hypocenters is shown in cross-section in Figure 7 where the seismicity in the surrounding 20 km of the EAF and the Cardak fault is shown for the Mw 7.8 mainshock and the Mw 7.6 aftershock, respectively. Despite uncertainties in hypocenter location due to a sparse seismic network, the distribution of aftershocks exhibits a remarkable complementarity with the distribution of coseismic slip, surrounding the regions of high slip, but also concentrating at segment boundaries. Additional aftershocks extend the ruptured faults outwards, past the rupture tip. This is the case near Antakya, where seismicity propagates towards the Cyprus Arc, east of the Karasu trough, where seismicity propagates towards the Dead Sea Fault, and north of the Sürgü fault, creating a new fault structure running parallel to the EAF.

The complementarity of the distribution of coseismic slip and aftershocks is another indication of the depth extent of the seismogenic zone. For the Mw 7.8 mainshock there is a dearth of aftershocks between 2 and 10 km depth. For the Mw 7.6 aftershock, the seismicity is much less intense between 2 and 8 km depth. The lateral variations in the depth extent of aftershocks may be associated with differences in hydrothermal conditions, such as geothermal gradients and pore fluid pressure, or with different compositions of the fault zones. We speculate that the seismogenic zone extends from 4 to 10 km depth in this region and that the coseismic slip that occurred outside these bounds took place in a nominally rate-strengthening region of the fault. Coseismic slip commonly propagates in regions of stable sliding because of dynamic effects (Barbot et al., 2012; Noda

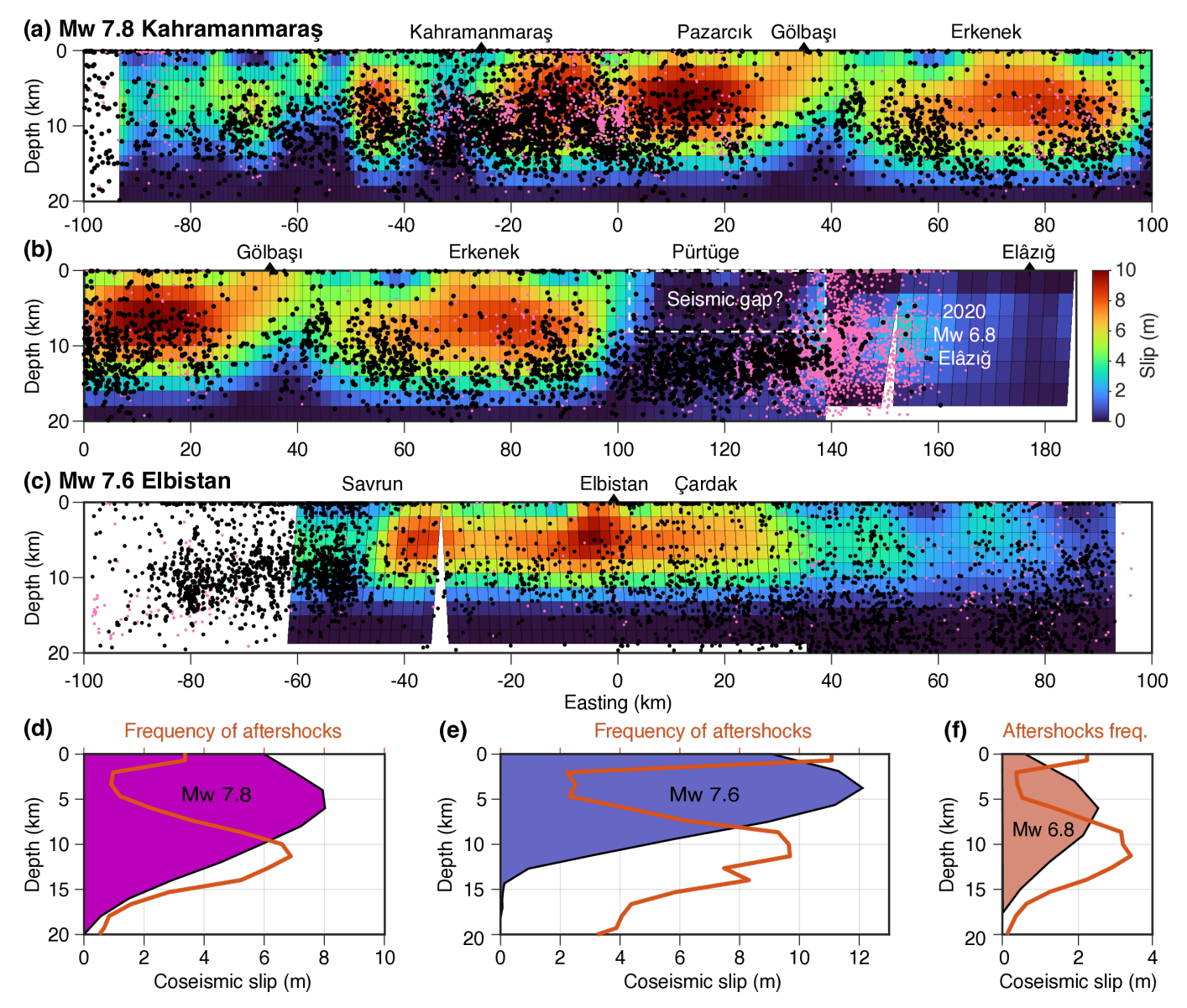


**Figure 7** Shallow slip deficit and potential seismic gap along the Pütürge segment. a) Coseismic slip distribution of the the 2023 February 6<sup>th</sup> Mw 7.8 Kahramanmaraş mainshock with peak slip between 6 and 8 km depth. b) Coseismic slip distribution of the Mw 7.8 mainshock in relation to the 2020 Mw 6.8 Elazığ earthquake (Pousse-Beltran et al., 2020a), highlighting a potential 40 km-long seismic gap in the Pütürge segment. c) Coseismic slip distribution of the 2023 February 6 Mw 7.6 Elbistan aftershock. The aftershocks distribution and the background microseismicity before the respective earthquakes are shown with black and purple dots, respectively. d) Depth distribution of coseismic slip and aftershocks for the Mw 7.8 mainshock, highlighting a shallow slip deficit. The aftershocks concentrate in regions of high gradient of slip. e) Same for the Mw 7.6 aftershock. f) Same for the 2020 Mw 6.8 Elazığ earthquake and its aftershocks.

# and Lapusta, 2013; Salman et al., 2017; Barbot, 2019b; Nanjundiah et al., 2020; Wang and Barbot, 2023).

The distribution of coseismic slip reveals asperities of large slip centered along the South Amanos, North Amanos, Pazarcık, and Erkenek segment separated by major releasing bends and step-overs (Duman and Emre, 2013). These segments ruptured in smaller-magnitude earthquakes in the last millennia. The Amanos segment hosted an Mw=7.5 earthquake in 521. The Pazarcık segment ruptured previously in 1513 in a Mw=7.4 earthquake. The Erkenek segment ruptured with a Mw=7.1 earthquake in 1893. Although all these segments ruptured in a single event during the Mw 7.8 mainshock, the waxing and waning of coseismic slip along the strike direction follows the same segmen-

tation, with tapering of fault slip near segment boundaries. This behavior is compatible with the start-stop control of fault bends and morphological gradients on seismicity (Qiu et al., 2016; Sathiakumar and Barbot, 2021).

A somewhat surprising behavior of the Kahramanmaraş earthquake sequence is the rupture of faults with the same sense of motion — left-lateral strike-slip — despite the high angle between the Çardak Fault and the Pazarcık-Erkenek segment that hosted much coseismic slip. Recent strike-slip earthquakes on oblique faults, such as the 2012 Mw 8.6 Indian Ocean (Wei et al., 2013; Masuti et al., 2016) or the 2019 Mw 7.2 Ridgecrest (Chen et al., 2020; Qiu et al., 2020) earthquakes occurred on conjugate faults, i.e., one being dextral while the other is sinistral. The activation of faults with the same sense of motion is not uncommon within the context of escape tectonics that operates in Anatolia. For example, the oblique Altyn Tagh Fault and the Kunlun Fault in Tibet accommodate the extrusion of southern Tibet.

A remaining question is how the Kahramanmaraş earthquake will affect future seismic unrest in the region. Of particular concern is the potential triggering of large earthquakes along the DSF system. However, the distribution of aftershocks and the fault orientation of the Mw 6.4 aftershock indicate propagation of seismic unrest toward the Cyprus Arc (Figures 1, 2, and 6). Nevertheless, intense seismicity concentrates along the eastern side of the Karasu trough, running parallel to the Amanos segment in the direction of the DSF. Hence, the potential of a southward propagation of seismicity is not entirely excluded.

More alarmingly, the slip distribution indicates a large remaining seismic gap in the Pütürge segment that separates the 2023 Mw 7.8 mainshock rupture and the fault area involved in the 2020 Mw 6.8 Elazığ earthquake (Figure 7b). The aftershock distribution connects the two ruptures between 10 and 20 km depth, leaving a 40 km-long seismic gap between the surface and 10 km depth. This area is similar to the 2020 rupture. Hence, we raise concern for the possibility of another Mw 6.8 earthquake to occur in the Pütürge segment of the EAF. Analysis of geodetic data across the Pütürge and Palu segment of the EAF indicate high interseismic coupling south of the 2020 Elazığ rupture (Bletery et al., 2020). Dedicated instrumentation is necessary to monitor the fault behavior in this region.

#### **Conclusions**

Remote sensing data provide great insights into the 2023 Kahramanmaraş earthquake sequence, including the extent of the surface rupture and the distribution of coseismic slip along various segments of the EAF and Çardak fault during the Mw 7.8 mainshock and the Mw 7.6 aftershock. The mainshock ruptured the Amanos, Pazarcık, and Erkenek segments propagating across fault bends and releasing step-overs. The southward rupture termination was caused by the diffuse termination of the EAF as it bifurcates into the Antakya Fault and the DSF. The second largest aftershock, the Antakya Mw 6.4 earthquake extends the rupture along the Antakya Fault toward the Mediterranean Basin, alleviating the risk of triggering large earthquakes on the DSF. To the north, the rupture propagation was arrested by the Yarpuzlu releasing bend at the southern boundary of the Pütürge segment of the EAF, leaving a 40 kmlong seismic gap to the rupture area of the 2020 Mw 6.8 Elazığ earthquake. The Pütürge segment must be instrumented to assess its seismic potential.

The Mw 7.6 Elbistan aftershock ruptured the nearby Çardak and Savrun faults and a previously unidentified fault situated across the Nurhak complexity between the Sürgü Fault and the Malatya Fault. The Mw 7.8 mainshock and the Mw 7.6 aftershock share the same sense of motion — left-lateral strike-slip faulting — despite markedly different fault orientations. The dis-

tribution of coseismic slip for both events highlights a pronounced shallow slip deficit and a complementarity with the aftershock distribution. These observations provide constraints on the depth of the seismogenic zone, defined as the area where large earthquakes nucleate and propagate. The depth distributions of aftershocks and of coseismic slip indicate an unstable-weakening region between 4 and 10 km depth. The Kahramanmaraş earthquake sequence reminds us of the devastating potential of immature strike-slip faults.

#### **Acknowledgments**

We are grateful for the constructive reviews of Romain Jolivet and the additional comments from the editors Edwin Nissen and Stephen Hicks. SB is supported in part by the National Science Foundation under award number EAR-1848192. YH is supported in part by the Israel Science Foundation, grant number ISF 2091/20. MTJ acknowledges funding of the PhD grant through the Prof. Maria Zadro legacy to the University of Trieste. CB acknowledges funding from MIUR-PRIN.

#### **Supplementary Information**

The supplementary information (Figures S1-S8 and Tables S1-S2) can be found at https://doi.org/10.5281/zenodo.7747846.

### **Competing interests**

There are no competing interests.

# **Data availability**

The Sentinel-1 SAR data and Sentinel-2 optical data are provided by the European Space Agency (https:// scihub.copernicus.eu) and are additionally distributed by the Alaska Satellite Facility (https://asf.alaska.edu/ how-to/data-tools). The Advanced Land Observation Satellite-2 (ALOS-2) SAR data used in this work are copyright Japan Aerospace Exploration Agency (JAXA) and are open accessed at https://www.eorc.jaxa.jp/ ALOS/en/dataset/alos\_open\_and\_free\_e.htm. The aftershock dataset is available at https://zenodo.org/record/ 7699882#.ZAjBfuzMI-Q. The Sentinel-2 cross-correlation of optical imagery is at http://doi.data-terra.u-strasbg.fr/ GDM\_OPT\_Turkey\_Syria/. The GNSS offsets are available in Tables S1 and S2. The slip distributions of the Mw 7.8 Kahramanmaras mainshock, Mw 7.6 Elbistan aftershock, Mw 6.4 Antakya aftershock, and of the 2020 Mw 6.8 Elazığ earthquake can be found at https: //doi.org/10.5281/zenodo.7747846.

#### References

Aktug, B., Ozener, H., Dogru, A., Sabuncu, A., Turgut, B., Halicioglu, K., Yilmaz, O., and Havazli, E. Slip rates and seismic potential on the East Anatolian Fault System using an improved GPS velocity field. *Journal of Geodynamics*, 94:1–12, 2016. doi: 10.1016/j.jog.2016.01.001.

- Ambraseys, N. *Earthquakes in the Mediterranean and Middle East: a multidisciplinary study of seismicity up to 1900.* Cambridge University Press, 2009. doi: 10.1017/CBO9781139195430.
- Ambraseys, N. N. Some Characteristic Features of the North Anatolian Fault Zone. *Tectonophysics*, 9:143–165, 1970.
- An, M., Zhang, F., Elsworth, D., Xu, Z., Chen, Z., and Zhang, L. Friction of Longmaxi shale gouges and implications for seismicity during hydraulic fracturing. *Journal of Geophysical Research: Solid Earth*, 125(8):e2020JB019885, 2020. doi: 10.1029/2020JB019885.
- Armijo, R., Meyer, B., Hubert, A., and Barka, A. Westward propagation of the North Anatolian fault into the northern Aegean: Timing and kinematics. *Geology*, 27(3):267–270, 1999. doi: 10.1130/0091-7613(1999)027<0267:WPOTNA>2.3.CO;2.
- Aster, R. C., Borchers, B., and Thurber, C. H. *Parameter estimation and inverse problems*. Academic Press, 2nd edition, 2012.
- Bagnardi, M. and Hooper, A. Inversion of surface deformation data for rapid estimates of source parameters and uncertainties: A Bayesian approach. *Geochemistry, Geophysics, Geosystems*, 19 (7):2194–2211, 2018.
- Barbot, S. Modulation of fault strength during the seismic cycle by grain-size evolution around contact junctions. *Tectonophysics*, 765:129–145, 2019a. doi: 10.1016/j.tecto.2019.05.004.
- Barbot, S. Slow-slip, slow earthquakes, period-two cycles, full and partial ruptures, and deterministic chaos in a single asperity fault. *Tectonophysics*, 768:228171, 2019b. doi: 10.1016/j.tecto.2019.228171.
- Barbot, S. and Weiss, J. Connecting subduction, extension and shear localization across the Aegean Sea and Anatolia. *Geophys. J. Int.*, 226(1):422–445, 2021. doi: 10.1093/gji/ggab078.
- Barbot, S., Fialko, Y., and Sandwell, D. Effect of a Compliant Fault Zone on the Inferred Earthquake Slip Distribution. *J. Geophys. Res.*, 113(B6), June 2008a. doi: 10.1029/2007JB005256.
- Barbot, S., Hamiel, Y., and Fialko, Y. Space geodetic investigation of the coseismic and postseismic deformation due to the 2003 Mw 7.2 Altai earthquake: Implications for the local lithospheric rheology. *J. Geophys. Res.*, 113(B03403), 2008b. doi: 10.1029/2007JB005063.
- Barbot, S., Fialko, Y., and Bock, Y. Postseismic Deformation due to the Mw 6.0 2004 Parkfield Earthquake: Stress-Driven Creep on a Fault with Spatially Variable Rate-and-State Friction Parameters. *J. Geophys. Res.*, 114(B07405), 2009a. doi: 10.1029/2008JB005748.
- Barbot, S., Fialko, Y., and Sandwell, D. Three-Dimensional Models of Elasto-Static Deformation in Heterogeneous Media, with Applications to the Eastern California Shear Zone. *Geophys. J. Int.*, 179(1):500–520, 2009b. doi: 10.1111/j.1365-246X.2009.04194.x.
- Barbot, S., Lapusta, N., and Avouac, J. P. Under the Hood of the Earthquake Machine: Towards Predictive Modeling of the Seismic Cycle. *Science*, 336(6082):707–710, 2012. doi: 10.1126/science.1218796.
- Barbot, S., Agram, P., and De Michele, M. Change of Apparent Segmentation of the San Andreas Fault Around Parkfield from Space Geodetic Observations Across Multiple Periods. *J. Geophys. Res.*, 118(12):6311–6327, 2013. doi: 10.1002/2013JB010442.
- Bilham, R., Ozener, H., Mencin, D., Dogru, A., Ergintav, S., Cakir, Z., Aytun, A., Aktug, B., Yilmaz, O., Johnson, W., et al. Surface creep on the North Anatolian fault at Ismetpasa, Turkey, 1944–2016. *J. Geophys. Res.*, 121(10):7409–7431, 2016. doi: 10.1002/2016JB013394.
- Blanpied, M. L., Lockner, D. A., and Byerlee, J. D. Frictional slip of granite at hydrothermal conditions. *J. Geophys. Res.*, 100(B7):

- 13045-13064, 1995. doi: 10.1029/95JB00862.
- Bletery, Q., Cavalié, O., Nocquet, J.-M., and Ragon, T. Distribution of interseismic coupling along the North and East Anatolian Faults inferred from InSAR and GPS data. *Geophys. Res. Lett.*, 47 (16):e2020GL087775, 2020. doi: 10.1029/2020GL087775.
- Bohnhoff, M., Martínez-Garzón, P., Bulut, F., Stierle, E., and Ben-Zion, Y. Maximum earthquake magnitudes along different sections of the North Anatolian fault zone. *Tectonophysics*, 674: 147–165, 2016. doi: 10.1016/j.tecto.2016.02.028.
- Boulton, C., Moore, D. E., Lockner, D. A., Toy, V. G., Townend, J., and Sutherland, R. Frictional properties of exhumed fault gouges in DFDP-1 cores, Alpine Fault, New Zealand. *Geophys. Res. Lett.*, 41 (2):356–362, 2014. doi: 10.1002/2013GL058236.
- Bozkurt, E. Neotectonics of Turkey-a synthesis. *Geodinamica acta*, 14(1-3):3-30, 2001. doi: 10.1080/09853111.2001.11432432.
- Bulut, F., Bohnhoff, M., Eken, T., Janssen, C., Kılıç, T., and Dresen, G. The East Anatolian Fault Zone: Seismotectonic setting and spatiotemporal characteristics of seismicity based on precise earthquake locations. *J. Geophys. Res.*, 117(B7), 2012. doi: 10.1029/2011JB008966.
- Cavalié, O. and Jónsson, S. Block-like plate movements in eastern Anatolia observed by InSAR. *Geophys. Res. Lett.*, 41(1):26–31, 2014. doi: 10.1002/2013GL058170.
- Cetin, E., Cakir, Z., Meghraoui, M., Ergintav, S., and Akoglu, A. M. Extent and distribution of aseismic slip on the Ismetpaşa segment of the North Anatolian Fault (Turkey) from Persistent Scatterer InSAR. *Geochemistry, Geophysics, Geosystems*, 15(7):2883–2894, 2014. doi: 10.1002/2014GC005307.
- Chen, C. and Zebker, H. Phase unwrapping for large SAR interferograms: statistical segmentation and generalized network models. *IEEE Trans. Geosci. Rem. Sens.*, 40(8):1709–1719, 2002.
- Chen, K., Avouac, J.-P., Aati, S., Milliner, C., Zheng, F., and Shi, C. Cascading and pulse-like ruptures during the 2019 Ridgecrest earthquakes in the Eastern California Shear Zone. *Nature communications*, 11(1):1–8, 2020. doi: 10.1038/s41467-019-13750-
- Cochran, Y., Li, Y.-G., Shearer, P., Barbot, S., Fialko, Y., and Vidale, J. Seismic and Geodetic Evidence For Extensive, Long-Lived Fault Damage Zones. *Geology*, 37(4):315–318, Apr. 2009. doi: 10.1130/G25306A.1.
- Dal Zilio, L. and Ampuero, J. Earthquake doublet in Turkey and Syria. *Comm. Earth Environ*, 4(71), 2023. doi: 10.1038/s43247-023-00747-z.
- den Hartog, S., Thomas, M. Y., and Faulkner, D. How do laboratory friction parameters compare with observed fault slip and geodetically derived friction parameters? Insights from the Longitudinal Valley Fault, Taiwan. *J. Geophys. Res.*, 126(10): e2021JB022390, 2021. doi: 10.1029/2021JB022390.
- Di Toro, G., Han, R., Hirose, T., Paola, N. D., Nielsen, S., Mizoguchi, K., Ferri, F., Cocco, M., and Shimamoto, T. Fault lubrication during earthquakes. *Nature*, 471:494–498, 2011. doi: 10.1038/nature09838.
- Duman, T. Y. and Emre, Ö. The East Anatolian Fault: geometry, segmentation and jog characteristics. *Geological Society, London, Special Publications*, 372(1):495–529, 2013. doi: 10.1144/SP372.1.
- Emre, O., Duman, T., Özalp, S., Şaroğlu, F., Olgun, c., Elmaci, H., and Can, T. Active fault database of Turkey. *Bulletin of Earthquake Engineering*, 16:3229–3275, 07 2018. doi: 10.1007/s10518-016-0041-2.
- Faccenna, C. and Becker, T. W. Shaping mobile belts by small-scale convection. *Nature*, 465(7298):602–605, 2010. doi: 10.1038/nature09064.

- Faccenna, C., Becker, T. W., Auer, L., Billi, A., Boschi, L., Brun, J. P., Capitanio, F. A., Funiciello, F., Horvàth, F., Jolivet, L., et al. Mantle dynamics in the Mediterranean. *Reviews of Geophysics*, 52 (3):283–332, 2014. doi: 10.1002/2013RG000444.
- Farr, T. G., Rosen, P. A., Caro, E., Crippen, R., Duren, R., Hensley, S., Kobrick, M., Paller, M., Rodriguez, E., Roth, L., et al. The shuttle radar topography mission. *Reviews of geophysics*, 45(2), 2007. doi: 10.1029/2005RG000183.
- Fialko, Y. Probing the mechanical properties of seismically active crust with space geodesy: Study of the co-seismic deformation due to the 1992  ${\rm M}_w 7.3$  Landers (Southern California) earthquake. *J. Geophys. Res.*, 109(B03307), 2004.
- Fialko, Y., Sandwell, D., Agnew, D., Simons, M., Shearer, P., and Minster, B. Deformation on nearby faults induced by the 1999 Hector Mine earthquake. *Science*, 297:1858–1862, 2002. doi: 10.1126/science.1074671.
- Fialko, Y., Sandwell, D., Simons, M., and Rosen, P. Threedimensional deformation caused by the Bam, Iran, earthquake and the origin of shallow slip deficit. *Nature*, 435:295–299, May 2005.
- ForM@Ter. ForMTer EOST (2023): Terrain displacement from the Turkiye-Syria earthquakes of February 6,2023 obtained with the GDM-OPT-ETQ service applied on Sentinel-2 optical imagery, 2023
- Garfunkel, Z., Zak, I., and Freund, R. Active faulting in the Dead Sea rift. *Tectonophysics*, 80(1-4):1–26, 1981. doi: 10.1016/0040-1951(81)90139-6.
- Güvercin, S. E., Karabulut, H., Konca, A. Ö., Doğan, U., and Ergintav, S. Active seismotectonics of the East Anatolian Fault. *Geophys. J. Int.*, 230(1):50–69, 2022. doi: 10.1093/gji/ggac045.
- Hamiel, Y. and Fialko, Y. Structure and mechanical properties of faults in the North Anatolian Fault system from InSAR observations of coseismic deformation due to the 1999 Izmit (Turkey) earthquake. *J. Geophys. Res.*, 112(B07412), 2007. doi: 10.1029/2006JB004777.
- Hamiel, Y. and Piatibratova, O. Spatial variations of slip and creep rates along the southern and central Dead Sea Fault and the Carmel–Gilboa Fault System. *J. Geophys. Res.*, 126(9): e2020JB021585, 2021. doi: 10.1029/2020JB021585.
- Hartleb, R. D., Dolan, J. F., Akyüz, H. S., and Yerli, B. A 2000-year-long paleoseismologic record of earthquakes along the central North Anatolian Fault, from trenches at Alayurt, Turkey. *Bull. Seism. Soc. Am.*, 93(5):1935–1954, 2003. doi: 10.1785/0120010271.
- Herring, T., King, R., Floyd, M., and McCluskey, S. Introduction to GAMIT/GLOBK. *Massachusetts Institute of Technology, Cambridge, Massachusetts*, page 54, 2018.
- Hubert-Ferrari, A., Armijo, R., King, G., Meyer, B., and Barka, A. Morphology, displacement, and slip rates along the North Anatolian Fault, Turkey. *J. Geophys. Res.*, 107(B10):ETG-9, 2002. doi: 10.1029/2001JB000393.
- Hubert-Ferrari, A., Lamair, L., Hage, S., Schmidt, S., Çağatay, M. N., and Avşar, U. A 3800 yr paleoseismic record (Lake Hazar sediments, eastern Turkey): Implications for the East Anatolian Fault seismic cycle. *Earth Planet. Sci. Lett.*, 538:116152, 2020. doi: 10.1016/j.epsl.2020.116152.
- Huiskamp, G. Difference formulas for the surface Laplacian on a triangulated surface. *J. Comp. Physics*, 95(2):477–496, 1991. doi: 10.1016/0021-9991(91)90286-T.
- Jackson, J. and McKenzie, D. Active tectonics of the Alpine– Himalayan belt between western Turkey and Pakistan. Geophys. J. Int., 77(1):185–264, 1984. doi: 10.1111/j.1365-246X.1984.tb01931.x.

- Javed, M. T., Barbot, S., Javed, F., Ali, A., and Braitenberg, C. Coseismic folding during ramp failure at the front of the Sulaiman fold-and-thrust belt. *Geophys. Res. Lett.*, page e2022GL099953, 2022. doi: 10.1029/2022GL099953.
- Jiang, J. and Lapusta, N. Deeper penetration of large earthquakes on seismically quiescent faults. *Science*, 352(6291):1293–1297, 2016.
- Jiang, J., Erickson, B. A., Lambert, V. R., Ampuero, J.-P., Ando, R., Barbot, S. D., Cattania, C., Zilio, L. D., Duan, B., Dunham, E. M., et al. Community-driven code comparisons for threedimensional dynamic modeling of sequences of earthquakes and aseismic slip. *J. Geophys. Res.*, 127(3):e2021JB023519, 2022. doi: 10.1029/2021JB023519.
- Jolivet, L., Faccenna, C., Huet, B., Labrousse, L., Le Pourhiet, L., Lacombe, O., Lecomte, E., Burov, E., Denèle, Y., Brun, J.-P., et al. Aegean tectonics: Strain localisation, slab tearing and trench retreat. *Tectonophysics*, 597:1–33, 2013. doi: 10.1016/j.tecto.2012.06.011.
- Jónsson, S., Zebker, H., Segall, P., and Amelung, F. Fault slip distribution of the 1999 M w 7.1 Hector Mine, California, earthquake, estimated from satellite radar and GPS measurements. *Bull. Seism. Soc. Am.*, 92(4):1377–1389, 2002. doi: 10.1785/0120000922.
- Kaneko, Y., Fialko, Y., Sandwell, D. T., Tong, X., and Furuya, M. Interseismic deformation and creep along the central section of the North Anatolian fault (Turkey): InSAR observations and implications for rate-and-state friction properties. *J. Geophys. Res.*, 118 (1):316–331, 2013. doi: 10.1029/2012JB009661.
- Konca, A. Ö., Karabulut, H., Güvercin, S. E., Eskiköy, F., Özarpacı, S., Özdemir, A., Floyd, M., Ergintav, S., and Doğan, U. From interseismic deformation with near-repeating earthquakes to co-seismic rupture: A unified view of the 2020 Mw 6. 8 Sivrice (Elazığ) Eastern Turkey earthquake. *J. Geophys. Res.*, 126(10): e2021JB021830, 2021. doi: 10.1029/2021JB021830.
- Lazecky, M., Spaans, K., González, P., Maghsoudi, Y., Morishita, Y., Albino, F., Elliott, J., Greenall, N., Hatton, E., Hooper, A., Juncu, D., McDougall, A., Walters, R., Watson, C., Weiss, J., and Wright, T. LiCSAR: An Automatic InSAR Tool for Measuring and Monitoring Tectonic and Volcanic Activity. *Remote Sensing*, 12(15):2430, 2020. doi: 10.3390/rs12152430.
- Le Pichon, X. and Kreemer, C. The Miocene-to-Present Kinematic Evolution of the Eastern Mediterranean and Middle East and Its Implications for Dynamics. *Annual Review of Earth and Planetary Sciences*, 38(1):323–351, 2010. doi: 10.1146/annurev-earth-040809-152419.
- Le Pichon, X., Şengör, A. C., Kende, J., İmren, C., Henry, P., Grall, C., and Karabulut, H. Propagation of a strike-slip plate boundary within an extensional environment: the westward propagation of the North Anatolian Fault. *Canadian Journal of Earth Sciences*, 53(11):1416–1439, 2016. doi: 10.1139/cjes-2015-0129.
- Leprince, S., Barbot, S., Ayoub, F., and Avouac, J. P. Automatic, Precise, Ortho-rectification and Coregistration for satellite Image Correlation, Application to Ground Deformation Measurement. *IEEE Trans. Geosc. Rem. Sens.*, 45(6):1529–1558, 2007. doi: 10.1109/TGRS.2006.888937.
- Liang, C., Agram, P., Simons, M., and Fielding, E. J. Ionospheric correction of InSAR time series analysis of C-band Sentinel-1 TOPS data. *IEEE Transactions on Geoscience and Remote Sensing*, 57 (9):6755–6773, 2019. doi: 10.1109/TGRS.2019.2908494.
- Liu, Y. and He, C. Friction properties of hornblende and implications for slow-slip events in subduction zones. *Tectonophysics*, 796:228644, 2020. doi: 10.1016/j.tecto.2020.228644.
- Lomax, A. Precise, NLL-SSST-coherence hypocenter catalog for the 2023 Mw 7.8 and Mw 7.6 SE Turkey earthquake sequence, March

2023.

- Lu, Z. and He, C. Frictional behavior of simulated biotite fault gouge under hydrothermal conditions. *Tectonophysics*, 622: 62–80, 2014. doi: 10.1016/j.tecto.2014.03.002.
- Lu, Z. and He, C. Friction of foliated fault gouge with a biotite interlayer at hydrothermal conditions. *Tectonophysics*, 740:72–92, 2018. doi: 10.1016/j.tecto.2018.05.003.
- Malinverno, A. and Ryan, W. B. Extension in the Tyrrhenian Sea and shortening in the Apennines as result of arc migration driven by sinking of the lithosphere. *Tectonics*, 5(2):227–245, 1986. doi: 10.1029/TC005i002p00227.
- Masuti, S., Barbot, S., Karato, S., Feng, L., and Banerjee, P. Upper mantle water stratification inferred from the 2012 Mw 8.6 Indian Ocean earthquake. *Nature*, 538:373–377, 2016. doi: 10.1038/nature19783.
- Melgar, D., Taymaz, T., Ganas, A., Crowell, B., Öcalan, T., Kahraman, M., Tsironi, V., Yolsal-Çevikbil, S., Valkaniotis, S., Irmak, T. S., Eken, T., Erman, C., Özkan, B., Dogan, A. H., and Altuntaş, C. Sub- and super-shear ruptures during the 2023 Mw 7.8 and Mw 7.6 earthquake doublet in SE Türkiye. Seismica, 2(3), Mar. 2023. doi: 10.26443/seismica.v2i3.387.
- Mitchell, E., Fialko, Y., and Brown, K. Velocity-weakening behavior of Westerly granite at temperature up to 600° C. *J. Geophys. Res.*, 121(9):6932–6946, 2016. doi: 10.1002/2016JB013081.
- Morishita, Y., Lazecky, M., Wright, T. J., Weiss, J. R., Elliott, J. R., and Hooper, A. LiCSBAS: An Open-Source InSAR Time Series Analysis Package Integrated with the LiCSAR Automated Sentinel-1 InSAR Processor. *Remote Sensing*, 12(3):424, 2020. doi: 10.3390/rs12030424.
- Nanjundiah, P., Barbot, S., and Wei, S. Static source properties of slow and fast earthquakes. *J. Geophys. Res.*, 125(12): e2019JB019028, 2020. doi: 10.1029/2019JB019028.
- Nazareth, J. J. and Hauksson, E. The seismogenic thickness of the southern California crust. *Bull. Seism. Soc. Am.*, 94(3):940–960, 2004. doi: 10.1785/0120020129.
- Nocquet, J.-M. Present-day kinematics of the Mediterranean: A comprehensive overview of GPS results. *Tectonophysics*, 579: 220–242, 2012. doi: 10.1016/j.tecto.2012.03.037.
- Noda, H. and Lapusta, N. Stable creeping fault segments can become destructive as a result of dynamic weakening. *Nature*, 493 (7433):518–521, 2013. doi: 10.1038/nature11703.
- Okada, Y. Internal Deformation Due to Shear and Tensile Faults in a Half-Space. *Bull. Seism. Soc. Am.*, 82:1018–1040, April 1992.
- Pousse-Beltran, L., Nissen, E., Bergman, E. A., Cambaz, M. D., Gaudreau, É., Karasözen, E., and Tan, F. The 2020 M w 6.8 Elazığ (Turkey) earthquake reveals rupture behavior of the East Anatolian Fault. *Geophys. Res. Lett.*, 47(13):e2020GL088136, 2020a. doi: 10.1029/2020GL088136.
- Pousse-Beltran, L., Socquet, A., Benedetti, L., Doin, M.-P., Rizza, M., and d'Agostino, N. Localized afterslip at geometrical complexities revealed by InSAR after the 2016 Central Italy seismic sequence. *J. Geophys. Res.*, 125(11):e2019JB019065, 2020b. doi: 10.1029/2019JB019065.
- Provost, F., Michéa, D., Malet, J.-P., Boissier, E., Pointal, E., Stumpf, A., Pacini, F., Doin, M.-P., Lacroix, P., Proy, C., et al. Terrain deformation measurements from optical satellite imagery: The MPIC-OPT processing services for geohazards monitoring. *Remote Sensing of Environment*, 274:112949, 2022. doi: 10.1016/j.rse.2022.112949.
- Qiu, Q., Hill, E. M., Barbot, S., Hubbard, J., Feng, W., Lindsey, E. O., Feng, L., Dai, K., Samsonov, S. V., and Tapponnier, P. The mechanism of partial rupture of a locked megathrust: The role of fault morphology. *Geology*, 44(10):875–878, 2016. doi:

- 10.1130/G38178.1.
- Qiu, Q., Barbot, S., Wang, T., and Wei, S. Slip complementarity and triggering between the foreshock, mainshock, and afterslip of the 2019 Ridgecrest rupture sequence. *Bull. Seism. Soc. Am.*, 110 (4):1701–1715, 2020. doi: 10.1785/0120200037.
- Rabinowitz, H., Savage, H., Skarbek, R., Ikari, M. J., Carpenter, B. M., and Collettini, C. Frictional behavior of input sediments to the Hikurangi Trench, New Zealand. *Geochemistry, Geophysics, Geosystems*, 19(9):2973–2990, 2018. doi: 10.1029/2018GC007633.
- Ragon, T., Simons, M., Bletery, Q., Cavalié, O., and Fielding, E. A stochastic view of the 2020 Elazig Mw 6.8 earthquake (Turkey). Geophys. Res. Lett., 48(3):e2020GL090704, 2021. doi: 10.1029/2020GL090704.
- Reilinger, R., McClusky, S., Vernant, P., Lawrence, S., Ergintav, S., Cakmak, R., Ozener, H., Kadirov, F., Guliev, I., Stepanyan, R., Nadariya, M., Hahubia, G., Mahmoud, S., Sakr, K., ArRajehi, A., Paradissis, D., Al-Aydrus, A., Prilepin, M., Guseva, T., Evren, E., Dmitrotsa, A., Filikov, S. V., Gomez, F., Al-Ghazzi, R., and Karam, G. GPS constraints on continental deformation in the Africa-Arabia-Eurasia continental collision zone and implications for the dynamics of plate interactions. *J. Geophys. Res.*, 111(B5), 2006. doi: 10.1029/2005JB004051.
- Reitman, N. G., Briggs, R. W., Barnhart, W. D., Jobe, J. A. T., DuRoss, C. B., Hatem, A. E., Gold, R. D., Mejstrik, J. D., , and Akçiz, S. Preliminary fault rupture mapping of the 2023 M7.8 and M7.5 Türkiye Earthquakes, 2023.
- Rice, J. R. and Ruina, A. L. Stability of steady frictional slipping. *J. Appl. Mech.*, **50**:343–349, **1983**. doi: 10.1115/1.3167042.
- Rollins, C., Barbot, S., and Avouac, J.-P. Postseismic deformation following the 2010 M=7.2 El Mayor-Cucapah earthquake: Observations, kinematic inversions, and dynamic models. *Pure Appl. Geophys.*, 172(5):1305–1358, 2015. doi: 10.1007/s00024-014-1005-6.
- Rollins, C., Avouac, J.-P., Landry, W., Argus, D. F., and Barbot, S. Interseismic strain accumulation on faults beneath Los Angeles, California. *J. Geophys. Res.*, 123(8):7126–7150, 2018. doi: 10.1029/2017JB015387.
- Rosen, P. A., Gurrola, E., Sacco, G. F., and Zebker, H. The InSAR scientific computing environment. In *EUSAR 2012; 9th European conference on synthetic aperture radar*, pages 730–733. VDE, 2012.
- Rosu, A.-M., Pierrot-Deseilligny, M., Delorme, A., Binet, R., and Klinger, Y. Measurement of ground displacement from optical satellite image correlation using the free open-source software MicMac. *ISPRS Journal of Photogrammetry and Remote Sensing*, 100:48–59, 2015. doi: 10.1016/j.isprsjprs.2014.03.002.
- Rousset, B., Barbot, S., Avouac, J. P., and Hsu, Y.-J. Postseismic Deformation Following the 1999 Chi-Chi Earthquake, Taiwan: Implication for Lower-Crust Rheology. *J. Geophys. Res.*, 117 (B12405):16, 2012. doi: 10.1029/2012JB009571.
- Rubin, A. M. and Ampuero, J.-P. Earthquake nucleation on (aging) rate and state faults. *J. Geophys. Res.*, 110(B11312):24 PP., 2005. doi: 10.1029/2005JB003686.
- Ruina, A. Slip instability and state variable friction laws. *J. Geophys. Res.*, 88:10,359–10,370, 1983. doi: 10.1029/JB088iB12p10359.
- Rupnik, E., Pierrot-Deseilligny, M., and Delorme, A. 3D reconstruction from multi-view VHR-satellite images in MicMac. *ISPRS Journal of Photogrammetry and Remote Sensing*, 139:201–211, 2018. doi: 10.1016/j.isprsjprs.2018.03.016.
- Ryan, W. B., Carbotte, S. M., Coplan, J. O., O'Hara, S., Melkonian, A., Arko, R., Weissel, R. A., Ferrini, V., Goodwillie, A., Nitsche, F., et al. Global multi-resolution topography synthe-

- sis. *Geochemistry, Geophysics, Geosystems*, 10(3), 2009. doi: 10.1029/2008GC002332.
- Salman, R., Hill, E. M., Feng, L., Lindsey, E. O., Mele Veedu, D., Barbot, S., Banerjee, P., Hermawan, I., and Natawidjaja, D. H. Piecemeal rupture of the Mentawai patch, Sumatra: The 2008 Mw 7.2 North Pagai earthquake sequence. *J. Geophys. Res.*, 122(11): 9404–9419, 2017. doi: 10.1002/2017JB014341.
- Sathiakumar, S. and Barbot, S. The stop-start control of seismicity by fault bends along the Main Himalayan Thrust. *Communications Earth & Environment*, 2(1):1–11, 2021. doi: 10.1038/s43247-021-00153-3.
- Sathiakumar, S., Barbot, S. D., and Agram, P. Extending resolution of fault slip with geodetic networks through optimal network design. *J. Geophys. Res.*, 122(12), 2017. doi: 10.1002/2017JB014326.
- Sawai, M., Niemeijer, A. R., Plümper, O., Hirose, T., and Spiers, C. J. Nucleation of frictional instability caused by fluid pressurization in subducted blueschist. *Geophys. Res. Lett.*, 43(6):2543–2551, 2016. doi: 10.1002/2015GL0675.
- Shearer, P., Hauksson, E., and Lin, G. Southern California hypocenter relocation with waveform cross-correlation, Part 2: Results using source-specific station terms and cluster analysis. *Bull. Seism. Soc. Am.*, 95(3):904–915, 2005.
- Takahashi, M., Uehara, S.-I., Mizoguchi, K., Shimizu, I., Okazaki, K., and Masuda, K. On the transient response of serpentine (antigorite) gouge to stepwise changes in slip velocity under high-temperature conditions. *J. Geophys. Res.*, 116(B10), 2011. doi: 10.1029/2010JB008062.
- Talebian, M. and Jackson, J. Offset on the Main Recent Fault of NW Iran and implications for the late Cenozoic tectonics of the Arabia–Eurasia collision zone. *Geophys. J. Int.*, 150(2):422–439, 2002. doi: 10.1046/j.1365-246X.2002.01711.x.
- Tang, C.-H., Barbot, S., Hsu, Y.-J., and Wu, Y.-M. Heterogeneous power-law flow with transient creep in southern California following the 2010 El Mayor-Cucapah earthquake. *J. Geophys. Res.*, 125(9):e2020JB019740, 2020. doi: 10.1029/2020JB019740.
- Taymaz, T., Jackson, J., and McKenzie, D. Active tectonics of the north and central Aegean Sea. *Geophys. J. Int.*, 106(2):433–490, 1991. doi: 10.1111/j.1365-246X.1991.tb03906.x.
- Tian, P. and He, C. Velocity weakening of simulated augite gouge at hydrothermal conditions: Implications for frictional slip of pyroxene-bearing mafic lower crust. *J. Geophys. Res.*, 124(7): 6428–6451, 2019. doi: 10.1029/2018JB016456.
- Valdez II, R., Kitajima, H., and Saffer, D. Effects of temperature on the frictional behavior of material from the Alpine Fault Zone, New Zealand. *Tectonophysics*, 762:17–27, 2019. doi: 10.1016/j.tecto.2019.04.022.
- Vernant, P., Nilforoushan, F., Hatzfeld, D., Abbassi, M., Vigny, C., Masson, F., Nankali, H., Martinod, J., Ashtiani, A., Bayer, R., et al. Present-day crustal deformation and plate kinematics in the Middle East constrained by GPS measurements in Iran and northern Oman. *Geophys. J. Int.*, 157(1):381–398, 2004. doi: 10.1111/j.1365-246X.2004.02222.x.
- Wang, B. and Barbot, S. Pulse-like ruptures, seismic swarms, and tremorgenic slow-slip events with thermally activated friction. *Earth Planet. Sci. Lett.*, 603:117983, 2023. doi: 10.1016/j.epsl.2022.117983.
- Wang, L. and Barbot, S. Excitation of San Andreas tremors by thermal instabilities below the seismogenic zone. *Science Advances*, 6(36):eabb2057, 2020. doi: 10.1126/sciadv.abb2057.
- Wang, T., Jónsson, S., and Hanssen, R. F. Improved SAR image coregistration using pixel-offset series. *IEEE geoscience and remote sensing letters*, 11(9):1465–1469, 2014. doi: 10.1109/L-

- GRS.2013.2295429.
- Wang, T., Shi, Q., Nikkhoo, M., Wei, S., Barbot, S., Dreger, D., Bürgmann, R., Motagh, M., and Chen, Q.-F. The rise, collapse, and compaction of Mt. Mantap from the 3 September 2017 North Korean nuclear test. *Science*, page eaar7230, 2018. doi: 10.1126/science.aar7230.
- Wei, S., Helmberger, D., and Avouac, J.-P. Modeling the 2012 Wharton basin earthquakes off-Sumatra: Complete lithospheric failure. *J. Geophys. Res.*, 118(7):3592–3609, 2013.
- Wei, S., Barbot, S., Graves, R., Lienkaemper, J. J., Wang, T., Hudnut, K., Fu, Y., and Helmberger, D. The 2014 Mw 6.1 South Napa earthquake: A unilateral rupture with shallow asperity and rapid afterslip. *Seism. Res. Lett.*, 86(2A):344–354, 2015. doi: 10.1785/0220140249.
- Wesnousky, S. G. Seismological and structural evolution of strike-slip faults. *Nature*, 335(6188):340–343, 1988. doi: 10.1038/335340a0.
- Yu, C., Li, Z., and Penna, N. T. Interferometric synthetic aperture radar atmospheric correction using a GPS-based iterative tropospheric decomposition model. *Remote Sensing of Environ*ment, 204:109–121, 2018a. doi: 10.1016/j.rse.2017.10.038.
- Yu, C., Li, Z., Penna, N. T., and Crippa, P. Generic atmospheric correction model for interferometric synthetic aperture radar observations. *J. Geophys. Res.*, 123(10):9202–9222, 2018b. doi: 10.1029/2017JB015305.

The article Slip distribution of the February 6, 2023 Mw 7.8 and Mw 7.6, Kahramanmaraş, Turkey earthquake sequence in the East Anatolian Fault Zone © 2023 by Sylvain Barbot is licensed under CC BY 4.0.